A Master Thesis

Background reduction of a cryogenic particle detector for dark matter detection

Kentaro Miuchi
Department of Physics, School of Science,
University of Tokyo

February 9, 1999

Abstract

In this thesis an attempt to reduce the background of a cryogenic particle detector, or bolometer is described. We have made a test running of the dark matter neutralino detection experiment in the surface laboratory with a LiF bolometer and learned that the background needs to be reduced by five orders of magnitude.

We decided to install our detector system in Nokogiriyama underground cell and measured the muon flux, gamma ray flux, and neutron flux there. Then we designed a veto system and passive shieldings for the underground experiment. We selected the materials for the passive shieldings from the viewpoint of the radioactive contamination. In the first experiment in Nokogiriyama underground cell, we obtained a result which sets the best limit for the spin-dependently interacting neutralino with a mass lighter than 5 GeV.

After the first measurement in Nokogiriyama underground cell, we studied the remaining background sources and found that muon induced particles and stray gamma rays make equal contribution to the background. We have improved the veto efficiency and constructed an internal shielding made of very low background lead. Because of an unexpected trouble of the dilution refrigerator, we have not performed the measurement with the constructed internal shielding yet.

Contents

1 Dark Matter Problem

1.1 Dark Matter Problem

A lot of observational information supports the hypothesis that at least 90 % of the mass in the universe consists of non-luminous matter which does not emit or absorb any form of electromagnetic radiation. This unknown matter is referred to as "dark matter", and many experiments are underway or prepared for the identification of this unknown "dark" matter.

Observation of the rotational velocity of stars and gas in galaxies offers us the clearest evidence of existence of dark matter. The rotational velocity is obtained by

$$m\frac{V(r)^2}{r} = G\frac{mM(r)}{r^2} \tag{1}$$

where G is the gravitational constant, r is the radial distance from the center of the galaxy, $M(r)$ is the total mass within a radius r. The rotational velocity is measured by observing atomic hydrogen clouds and is found to be constant up to far edge of the galaxy where luminous matter does not exist any more(Fig. 1). These observational result imply that $M(r)$ is proportional to r, that is an evidence of a large amount of non-luminous matter in the galaxy.

1.2 Candidates for the Dark Matter

The evidence of the dark matter offered physicists another problem; 'what does it consist of?'. There are two types of candidates: baryonic particles and non-baryonic ones.

1.2.1 Baryonic Candidates

It is natural to presume that the dark matter is made of baryons such as old stars, comets, planets, asteroids, or intergalactic gases. The Big Bang Nucleosynthesis(BBN) is a well-known theory which explains the early universe ($\sim$ 1 sec) well and successfully predicts the abundance of light elements: ^{4}He, ^{3}He, ^{2}H, ^{6}Li, Be, and B. According to BBN, the baryonic density parameter Ω_b(=baryonic density/critical density) is restricted in the range of $\Omega_b = 0.05 \pm 0.005$[3]. This value is well consistent with the observational result by COBE Far-Infrared Absolute Spectrometer, which gives $\Omega_b = 0.045 \pm 0.003$[4]. The observed luminous baryons give the luminous baryonic density $\Omega_{\text{luminous}} \sim 0.005$, that claims a large fraction of baryons may be unseen.(Fig. 2)

Paczynski[5] suggests to detect MAssive Compact Halo Object(MACHO) using gravitational microlensing. The microlensing effect is based on the fact that when a massive object is at a distance r from the line of sight to a star,

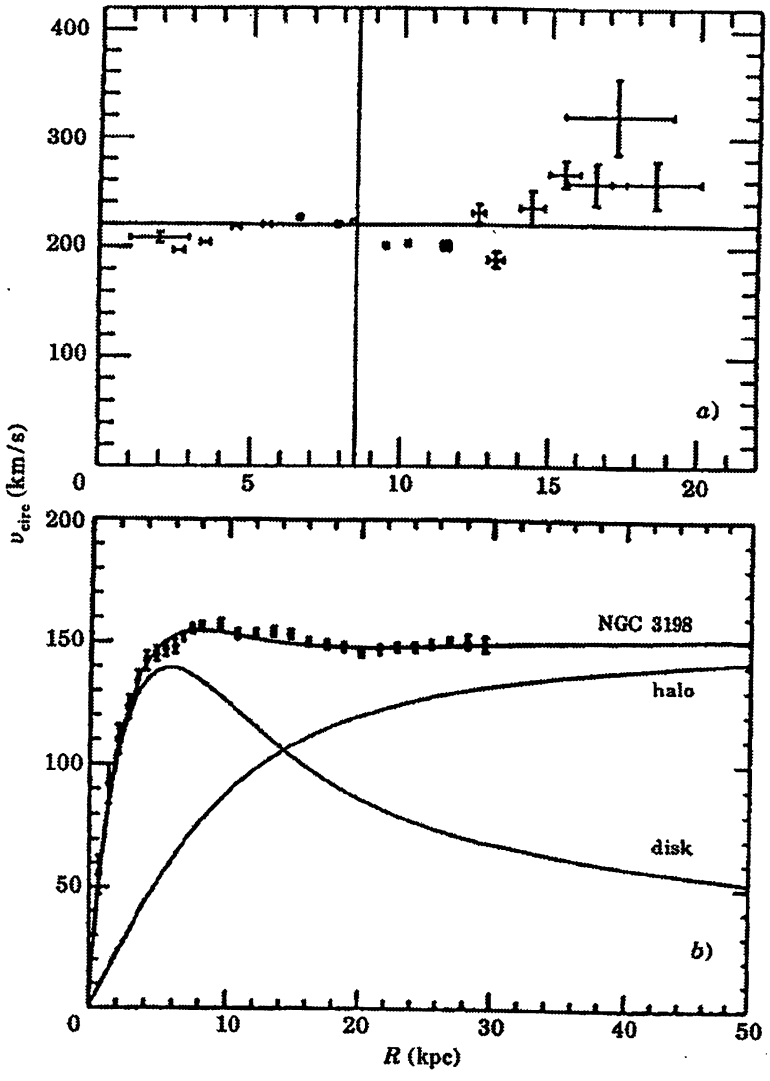

Figure 1: a)Mean rotational curve of our Galaxy[1]; b) rotational curve for NGC 3198 and predictions for disk and halo contributions[2]

the observer receives a light amplified by a factor

$$A = \frac{(u^2+2)}{(u\sqrt{u^2+4})} \tag{2}$$

where u is the ratio between r and the Einstein radius $R_E = (2/c)\sqrt{GML}\sqrt{x(1-x)}$; here M is the deflector mass, L and x times L are, respectively, the star and deflector distance to the observer. Three experiments are monitoring the light from the stars in Large Magelannic Cloud(LMC) and Galactic Bulge(GB)[7, 8, 9]. These observation suggests that the MACHOs do not constitute more than 30% of the galactic halo.

1.2.2 Non-Baryonic Candidates

Although some of the baryonic candidates have been found to occupy a part of dark matter, another solution is still needed to obtain $\Omega = 1$, which is an essential consequence of inflation theory. Many exotic candidates have been considered(Table 1). These candidates can be classified into hot dark matter(HDM) and cold dark matter (CDM); the former one is particle relativistic at decoupling time with masses less than $\approx$ 100 eV, while the latter is either relic particle non-relativistic at temperature greater than 10^4K with masses from few GeV to 10^{19}GeV or axions generated by symmetry breaking during the primordial Universe. By the cosmic microwave background radiation measurements of COBE, a mixed dark matter with composition of 30% HDM and 70% CDM is suggested. Among these candidates, light neutrino, axion, and neutralino are thought to be the most plausible ones[10].

- Light neutrino
  Light but not massless neutrino is a HDM candidate. The evidence for oscillation of atmospheric neutrinos presented by the Super-Kamiokande Collabolation[11] indicates that neutrino has mass and the lower limit of the mass indicates that neutrino contributes to the density of the universe at least as much as bright stars[13]. Though neutrino was found to contribute certain fraction of the mass in the universe, it cannot be the only non-baryonic dark matter; the failure of hot dark matter model of structure formation sets upper limit to the density parameter contributed by neutrino(Fig. 2).

- Axion
  Axion is light boson proposed by Peccei and Quinn [12] in 1977 which can solve the strong CP violation problem. With mass in the range $10^{-2} \sim 10^{-5}$eV, axion can close the universe as CDM.

- Neutralino
  Neutralino is the lightest supersymmetric particle(LSP) and is a promising

Theories and models	Candidate
GUT	massive neutrino magnetic monopole
SUSY	neutralino sneutrino gravitino gluino
Peccei-Quinn	axion
symmetry breaking	Majoron;Goldstone boson
exotics on galaxies formation	cosmic strings
exotics on matter constitution	SIMPs, quarks nuggets, nuclearites

Table 1: Non-baryonic dark matter candidates

CDM candidate. As this is the target of our dark matter search experiment, details are discussed in Section 2.

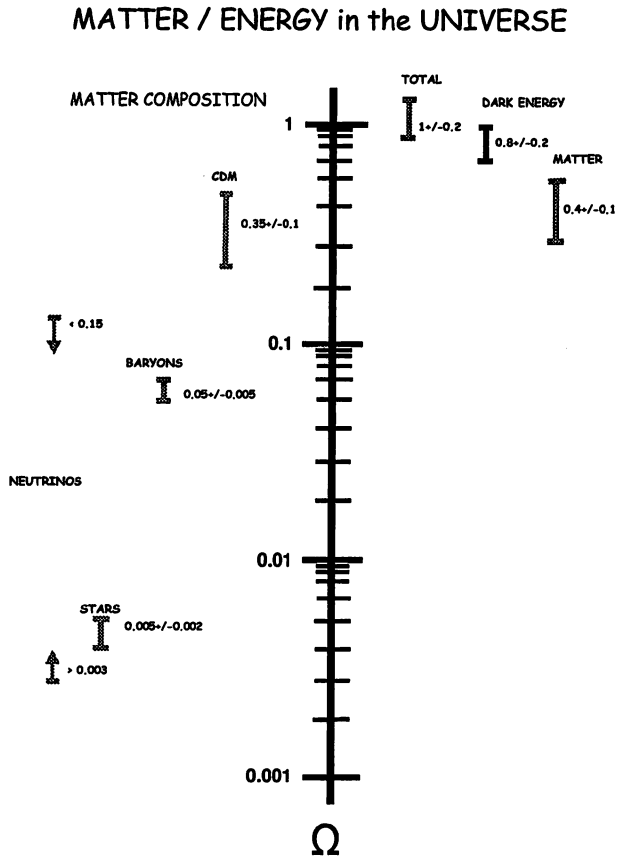

Figure 2: Summary of matter/energy in the Universe[13]. The right side refers to an overall accounting of matter and energy; the left refers to the composition of the matter component. Here, $65\,\mathrm{km}^{-1}\mathrm{Mpc}^{-1}$ is taken as Hubble constant H_0.

2 Neutralino-Nucleus Interaction

2.1 SUSY

The standard model is a non-Abelian gauge theory based on the gauge group $SU(3)_C \times SU(2)_L \times U(1)_Y$. Although standard model is a very successful theory which describes all experimental results with surprising accuracy, there are some questions remaining unanswered which can be solved with the supersymmetric extension of the standard model. Some of the questions are;

- standard model requires at least 18 free input parameters(fermion masses, $\sin^2\theta_W$, etc.).
- There is no framework where the gravity is incorporated.
- The Hierarchy Problem exists.

Among the several questions, the Hierarchy Problem is the most embarrassing one to the standard model and is the direct motivation to require supersymmetric extension. Radiative corrections to the scalar Higgs boson masses and gauge boson masses have quadratic divergences at large loop momentum. The energy cut-off Λ is required to avoid this divergences. For Higgs boson masses,

$$\begin{aligned} M_H^2 &= M_0^2 + \delta M_H^2 \\ \delta M_H^2 &\sim g^2\Lambda^2 \end{aligned} \tag{3}$$

where M_0 is the bare mass of the Higgs boson, δM_H is the mass correction. The experimental results suggests $M_{\rm H} = 150^{+150}_{-80}$GeV[14]. On the other hand, it is natural to consider the cut-off energy to be the GUT scale $\sim 10^{15}$GeV or the Plank scale $\sim 10^{19}$GeV, that means the correction is many orders of magnitude larger than the mass itself. SUSY model provides a solution to this Hierarchy problem. In SUSY model, the loop corrections to the Higgs boson masses contain the contributions of both fermions and bosons. Since supersymmetry is not an exact symmetry below a typical SUSY breaking scale M_{SUSY}, two contributions do not exactly cancel out: i.e.

$$\delta M_H^2 \sim O(10^{-2}) M_{SUSY}^2 \tag{4}$$

We can estimate the typical SUSY mass scale from requiring the Higgs boson mass is stable against its radiative correction: i.e. $\delta M_H < M_H$. From Eq.(3) and Eq.(4), we obtain

$$M_{SUSY} \leq 1\text{TeV}. \tag{5}$$

In SUSY model, each elementary particle with spin j in standard model has supersymmetric partner with spin $j-1/2$. The other internal quantum numbers are identical with those in the standard model. The particles presupposed in SUSY model are shown in Table 2.

spin	0			1/2			1
quark	squark			quark			
	$\begin{pmatrix} \tilde{u}_L \\ \tilde{d}_L \end{pmatrix}$	$\begin{pmatrix} \tilde{c}_L \\ \tilde{s}_L \end{pmatrix}$	$\begin{pmatrix} \tilde{t}_L \\ \tilde{b}_L \end{pmatrix}$	$\begin{pmatrix} u_L \\ d_L \end{pmatrix}$	$\begin{pmatrix} c_L \\ s_L \end{pmatrix}$	$\begin{pmatrix} t_L \\ b_L \end{pmatrix}$	
	$\tilde{u}_R$	$\tilde{c}_R$	$\tilde{t}_R$	u_R	c_R	t_R	
	$\tilde{d}_R$	$\tilde{s}_R$	$\tilde{b}_R$	d_R	s_R	b_R	
lepton	slepton			lepton			
	$\begin{pmatrix} \tilde{\nu}_L \\ \tilde{e}_{eL} \end{pmatrix}$	$\begin{pmatrix} \tilde{\nu}_{\mu L} \\ \tilde{\mu}_L \end{pmatrix}$	$\begin{pmatrix} \tilde{\nu}_{\tau L} \\ \tilde{\tau}_L \end{pmatrix}$	$\begin{pmatrix} \nu_{eL} \\ e_L \end{pmatrix}$	$\begin{pmatrix} \nu_{\mu L} \\ \mu_L \end{pmatrix}$	$\begin{pmatrix} \nu_{\tau L} \\ \tau_L \end{pmatrix}$	
	$\tilde{e}_R$	$\tilde{\mu}_R$	$\tilde{\tau}_R$	e_R	μ_R	τ_R	
higgs	higgs			higgsino			
	$\begin{pmatrix} H_1^0 \\ H_1^- \end{pmatrix}$ $\begin{pmatrix} H_2^+ \\ H_2^0 \end{pmatrix}$			$\begin{pmatrix} \tilde{H}_{1L}^0 \\ \tilde{H}_{1L}^- \end{pmatrix}$ $\begin{pmatrix} \tilde{H}_{2L}^+ \\ \tilde{H}_{2L}^0 \end{pmatrix}$			
				gaugino			gauge boson
				$\tilde{\gamma}$			γ
				$\tilde{Z}$ $\tilde{W}^{\pm}$			Z $W^{\pm}$
				$\tilde{g}$			g

Table 2: Particles presupposed in SUSY model.

2.2 Neutralino

In minimum supersymmetric extension of standard model(MSSM), the interaction between SUSY particle and ordinary particle is governed by 'R-Parity'. R-parity is defined as,

$$R = (-1)^{3B+L+2S} \tag{6}$$

where B is the baryon number, L is the lepton number and S is the spin. SUSY particles are assigned odd R-parity and the ordinary matter particles are assigned even R-parity. According to the R-parity conservation, heavier SUSY particles decay into lighter ones and the lightest supersymmetric particle(LSP) is stable because the decay into the ordinary particles violates R-parity conservation.

Neutralino (χ), the lowest-mass linear combination of photino($\tilde{\gamma}$), zino($\tilde{\mathrm{Z}}$) and higgsinos($\tilde{\mathrm{H}}_1^0, \tilde{\mathrm{H}}_2^0$) is the leading candidate for LSP and also for the non-baryonic cold dark matter. χ can be written as:

$$\chi = a_1\tilde{\gamma} + a_2\tilde{Z} + a_3\tilde{H}_1^0 + a_4\tilde{H}_2^0 \tag{7}$$

photino and zino are :

$$\begin{aligned} \tilde{\gamma} &= \cos\theta_W \tilde{B} + \sin\theta_W \tilde{W}^0 \\ \tilde{\mathrm{Z}} &= -\sin\theta_W \tilde{B} + \cos\theta_W \tilde{W}^0 \end{aligned} \tag{8}$$

where θ_W is the Weinberg angle, $\tilde{\mathrm{B}}$ and $\tilde{W}^0$ are superpartners of gauge bosons B and W^0 respectively. Neutralino mass matrix is

$$\begin{pmatrix} M_1 & 0 & -M_Z\cos\beta\sin\theta_W & M_Z\cos\beta\cos\theta_W \\ 0 & M_2 & M_Z\sin\beta\sin\theta_W & -M_Z\sin\beta\cos\theta_W \\ -M_Z\cos\beta\sin\theta_W & M_Z\sin\beta\sin\theta_W & 0 & -\mu \\ M_Z\cos\beta\cos\theta_W & -M_Z\sin\beta\cos\theta_W & -\mu & 0 \end{pmatrix} \tag{9}$$

The neutralino mass matrix has several parameters: the gaugino mass M_1 and M_2, the higgsino mass parameter μ, and $\tan\beta = v_2/v_1$, where v_1 and v_2 are the vacuum expectation values of the two Higgses present in the model. With the assumption of grand unification, $M_1 = (5/3)M_2$ is obtained, thus the neutralino mass matrix is characterized by three parameters, μ, M_2, and $\tan\beta$. Figure 3 and 4 show the contours of the mass and the gaugino fraction in the (μ, M_2) plane.

2.3 Neutralino-Nucleus Elastic Scattering

SUSY particle dark matter neutralino can be directly detected by neutralino-nucleus elastic scattering. In this section, the kinematics of the elastic scattering is discussed. First, the total event rates and energy spectra of zero-momentum transfer scattering are discussed. Then the cross sections and the form factor corrections is described. Details are reviewed in Ref.[15, 16, 17]

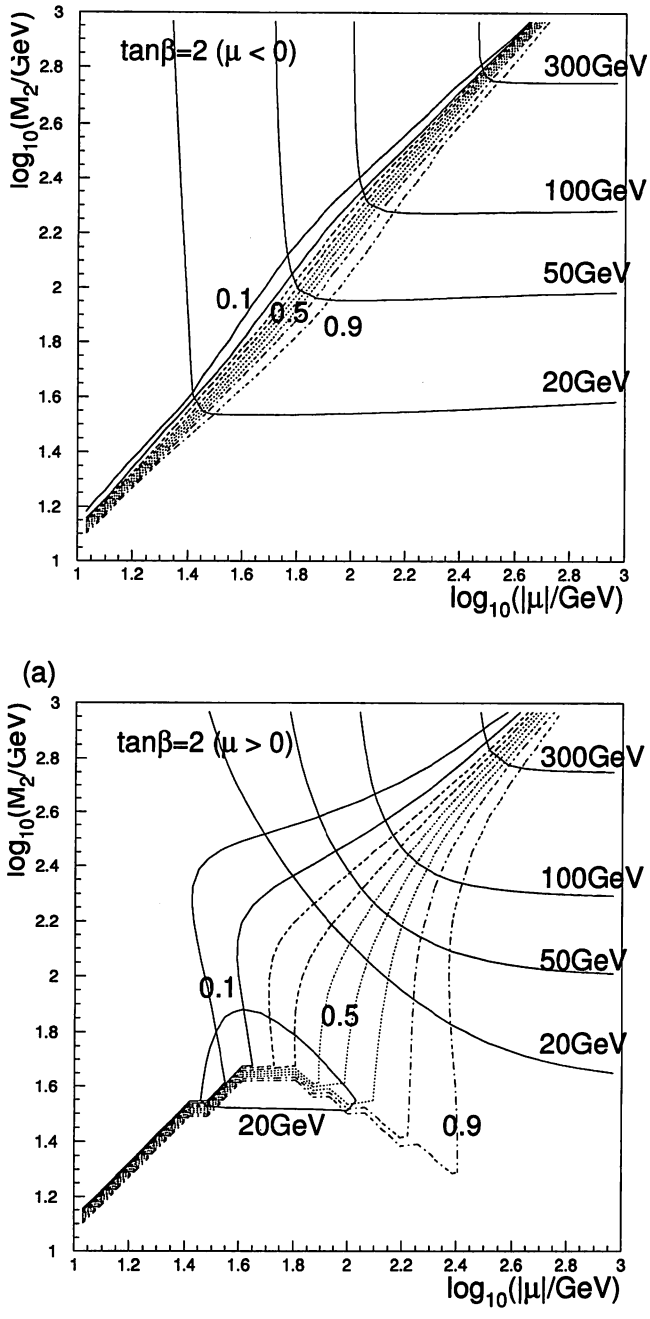

Figure 3: Contours of the mass and gaugino fraction. ($\tan\beta = 2$)[34]

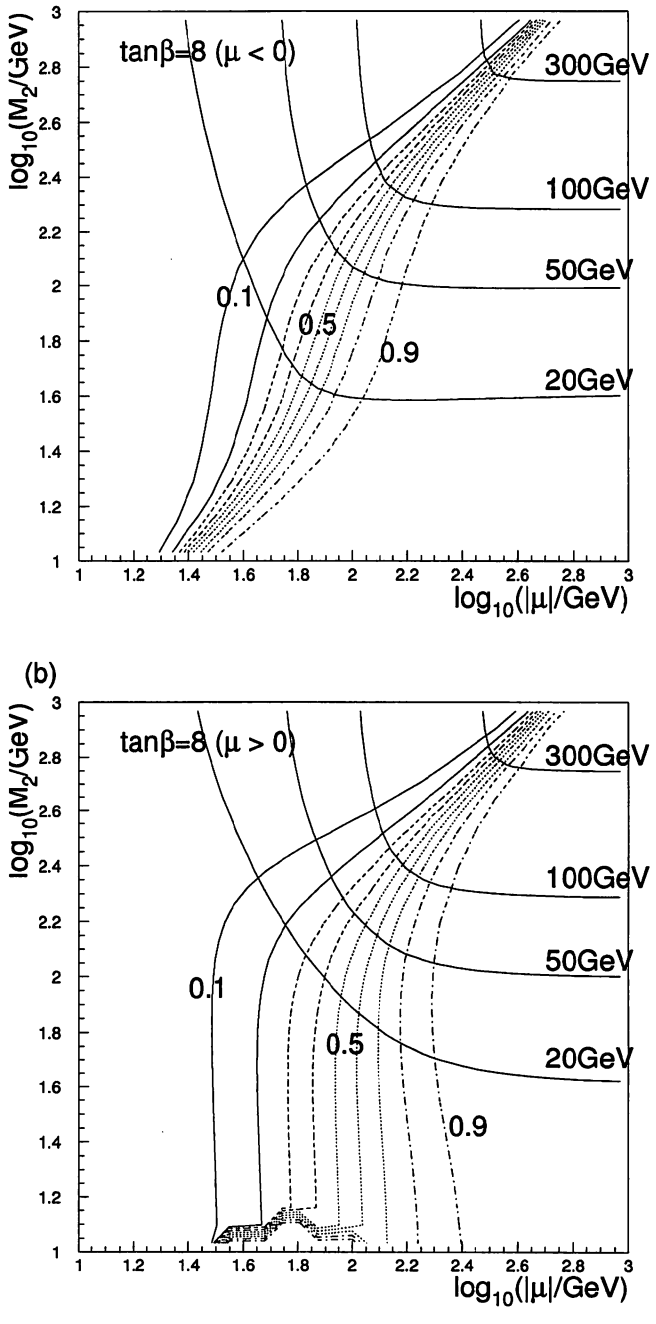

Figure 4: Contours of the mass and gaugino fraction. ($\tan\beta = 8$)[34]

2.3.1 Kinematics of Low Momentum Transfer Scattering

Differential particle density is given by:

$$\frac{dn}{d^3\vec{v}} = 4\pi \cdot \frac{n_0}{k} \cdot f(\vec{v}, \vec{v}_E) \tag{10}$$

where v_E is Earth velocity relative to the dark matter, k is the normalization constant. For the local Galactic escape velocity $v_{\rm esc} = \infty$,

$$k = k_0 = (\pi v_0^2)^{3/2} \tag{11}$$

n_0 is the mean dark matter particle number density:

$$n_0 = \frac{\rho_D}{M_D} \tag{12}$$

ρ_D is the dark matter density and M_D is the dark matter particle mass. As the dark matter velocity, Maxwellian distribution is assumed:

$$f(\vec{v}, \vec{v_E}) = e^{-|\vec{v}+\vec{v_E}|^2/v_0^2} \tag{13}$$

using Eq.(10)–Eq.(13), we obtain:

$$\frac{dn}{d^3\vec{v}} = n_0 \cdot (\pi v_0^2)^{-3/2} \cdot e^{-|\vec{v}+\vec{v_E}|^2/v_0^2} \tag{14}$$

where $\rho_D = 0.4 \mathrm{GeVc^{-2}cm^{-3}}$ is recent estimation by Gates et al.[18].

The event rate per unit mass is written as:

$$R = \frac{N_A}{A} \sigma n_0 \langle v \rangle \tag{15}$$

where A is a target atomic mass in units of AMU, N_A is the Avogadro number ($6.02 \cdot 10^{26} \mathrm{kg^{-1}}$), v is the dark matter velocity and σ is cross section per nucleus. For the discussion on zero momentum transfer scattering, σ = constant = σ_0 is assumed. Here we define R_0 as event rate per unit mass for $v_E = 0$ and $v_{esc} = \infty$; i.e.:

$$R_0 = \frac{2}{\pi^{1/2}} \cdot \frac{N_A}{A} \cdot \frac{\rho_D}{M_D} \sigma_0 v_0 \tag{16}$$

using Eq.(14) and Eq.(16), Eq.(15) can be written as

$$R = R_0 \cdot \frac{\pi^{1/2}}{2} \cdot \frac{\langle v \rangle}{v_0} = R_0 \cdot \frac{k_0}{k} \cdot \frac{1}{2\pi v_0^4} \cdot \int v f(\vec{v}, \vec{v}_E) d^3\vec{v} \tag{17}$$

for non zero v_E, Eq.(17) is:

$$\frac{R(v_E)}{R_0} = \frac{1}{2} \left[\pi^{1/2} \left(\frac{v_E}{v_0} + \frac{1}{2} \frac{v_0}{v_E} \right) \mathrm{erf} \left(\frac{v_E}{v_0} \right) + e^{-v_E^2/v_0^2} \right] \tag{18}$$

where $\mathrm{erf}(x) = 2/\pi^{1/2} \int_0^x \exp(-t^2)dt$ is the error function. The earth velocity v_E varies during the year as the Earth moves around the Sun. For practical purposes,

$$v_E \sim 244 + 15\sin(2\pi y)\mathrm{km\,s^{-1}} \tag{19}$$

where y is the elapsed time from March 2nd, in years. Eq.(17) is used later in differential form:

$$dR = R_0 \cdot \frac{k_0}{k} \cdot \frac{1}{2\pi v_0^4} v f(\vec{v}, \vec{v}_E) d\vec{v} \tag{20}$$

R_0 is conventionally expressed in units $\mathrm{kg^{-1}d^{-1}}$. Normalized to $\rho_D = 0.4\mathrm{GeVc^{-2}cm^{-3}}$ and v_0=230km $\mathrm{s^{-1}}$, Eq.(16) becomes:

$$R_0 = \frac{503}{M_D M_T} \left(\frac{\sigma_0}{1\mathrm{pb}}\right) \left(\frac{\rho_D}{0.4\mathrm{GeVc^{-2}cm^{-3}}}\right) \left(\frac{v_0}{230\mathrm{km\,s^{-1}}}\right) \tag{21}$$

with M_D, M_T in $\mathrm{GeVc^{-2}}$.

The recoil energy E_R of a nucleus struck by a dark matter particle of kinetic energy E, scattered at angle θ(in center-of-mass) is:

$$E_R = Er(1 - \cos\theta)/2 \tag{22}$$

where

$$r = 4M_D M_T/(M_D + M_T)^2. \tag{23}$$

With an assumption that the scattering is isotropic, i.e. uniform in $\cos\theta$, recoils are uniformly distributed in E_R over the range $0 \le E_R \le Er$; hence

$$\frac{dR}{dE_R} = \int_{E_{\min}}^{E_{\max}} \frac{1}{Er} dR(E) = \frac{1}{E_0 r} \int_{v_{\min}}^{v_{\max}} \frac{v_0^2}{v^2} dR(v) \tag{24}$$

using Eq.(20) and Eq.(24), we have:

$$\frac{dR}{dE_R} = \frac{R_0}{E_0 r} \frac{k_0}{k} \frac{1}{2\pi v_0^2} \int_{v_{\min}}^{v_{\max}} \frac{1}{v} f(\vec{v}, \vec{v}_E) dv \tag{25}$$

where $v_{\min} = (E_R/E_0 r)^{1/2} v_0$. From Eq.(25), nuclear recoil spectrum is obtained.

$$\frac{dR(v_E, \infty)}{dE_R} = \frac{R_0}{E_0 r} \frac{\pi^{1/2}}{4} \frac{v_0}{v_E} \left[\mathrm{erf}\left(\frac{v_{\min} + v_E}{v_0}\right) - \mathrm{erf}\left(\frac{v_{\min} - v_E}{v_0}\right)\right] \tag{26}$$

$$\sim c_1 \frac{R_0}{E_0 r} e^{-c_2 E_R/E_0 r} \tag{27}$$

Eq.(26) is approximated as Eq.(27) with $c_1 = 0.751$ and $c_2 = 0.561$. The expected recoil spectra of proton are shown in Figure 5.

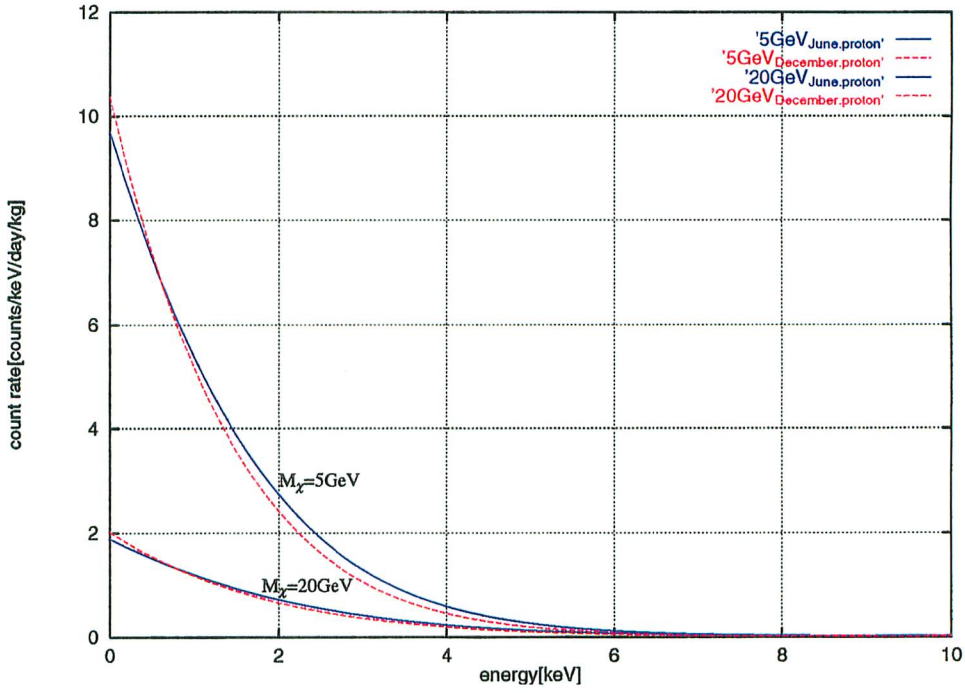

Figure 5: Expected recoil spectra of proton for M_χ=5 and 20GeV with seasonal modulation for both spectra. Here we take $\sigma_{\chi-p}$=0.1pb, v_0=230km s^{-1}, and $\rho_{\rm D} = 0.4{\rm GeV\,cm^{-3}}$.

2.3.2 Cross Sections

The neutralino-nucleus scattering could occur through spin-independent(coherent) or spin-dependent interaction. The cross section which determines the count rate depends strongly upon the nucleus and, even for the same nucleus, spin-independent cross section and spin-independent cross section generally have different values. The cross section of χ-nucleus elastic scattering is written as:

$$\sigma_{\chi-N} = \sigma_{\chi-p} \frac{\mu_N^2}{\mu_p^2} \frac{I_{CN}}{I_{Cp}} \tag{28}$$

where $\sigma_{\chi-p}$ is χ-proton cross section, μ_{N}^2 is the reduced mass of neutralino + target nucleus, and I_{CN} is a factor which effectively determines the cross section. The values of I_{CN} are discussed below.

- Spin-independent interactions
  In the spin-independent case, the dominant effect is the coherent sum of the scattering amplitudes on all the nucleons which, for sufficiently low momentum transfer ($qr_n \ll 1$), would add in phase to give a coherent cross section $\propto A^2$. If all nucleons participate equally, $I_{CN} = A^2$, and $I_{CN} \approx (A-Z)^2$ in the case of Dirac neutrinos for which the neutron interaction dominates.

- Spin-dependent interactions
  In the spin-dependent case, I is written as $I_{CN} = C^2\lambda^2 J(J+1)$. The values of $\lambda^2 J(J+1)$ calculated on the basis of single particle model and odd group model for various nuclei are listed in Table 3. C is a factor related to the quark spin content of the nucleon:

$$C = \sum_{q=u,d,s} T_q^3 \Delta q \tag{29}$$

  where Δq is the fraction of the nucleon spin factor by quark species q and $T_{u,d,s}^3 = \frac{1}{2}, -\frac{1}{2}, -\frac{1}{2}$, is the third component of isotopic spin for the respective quarks. For the comparison of the experimental result, the important thing is relative sensitivity of odd-N(Ge,Xe,Ga) and odd-Z(Na,I,F) targets. Here N represents neutron number. According to the calculation by European Muon Collaboration[19], the ratio C_{Wn}^2/C_{Wp}^2 are conveniently ~ 0.5 and we can practically use:

$$C_(\chi N)/C_(\chi p) = \begin{cases} 1 & \text{unpaired proton} \\ 0.5 & \text{unpaired neutron} \end{cases} \tag{30}$$

(a)unpaired proton				
			$\lambda^2 J(J+1)$	
Isotope	J	Abundance(%)	Odd group	Single particle
^{1}H	1/2	100	0.750	0.750
^{7}Li	3/2	92.5	0.411	0.417
^{19}F	1/2	100	0.647	0.75
^{23}Na	3/2	100	0.041	0.35
^{27}Al	5/2	100	0.087	0.35
^{35}Cl	3/2	75.8	0.036	0.15
^{51}V	7/2	99.8	0.167	0.321
^{69}Ga	3/2	60.1	0.021	0.417
^{71}Ga	3/2	39.9	0.089	0.417
^{75}As	3/2	100	0.000	0.417
^{93}Nb	9/2	100	0.162	0.306
^{107}Ag	1/2	57.8	0.054	0.083
^{109}Ag	1/2	48.2	0.057	0.083
^{127}I	5/2	100	0.023	0.250

(b)unpaired neutron				
			$\lambda^2 J(J+1)$	
Isotope	J	Abundance(%)	Odd group	Single particle
^{3}He	1/2	100	0.928	0.750
^{29}Si	1/2	4.7	0.063	0.750
^{67}Zn	5/2	4.1	0.073	0.179
^{73}Ge	9/2	7.8	0.065	0.306
^{99}Ru	5/2	12.7	0.039	0.350
^{101}Ru	5/2	17.0	0.049	0.350
^{111}Cd	1/2	12.8	0.072	0.750
^{113}Cd	1/2	12.2	0.079	0.750
^{115}Sn	1/2	0.4	0.173	0.750
^{117}Sn	1/2	7.7	0.205	0.750
^{129}Xe	1/2	26.4	0.124	0.750
^{131}Xe	3/2	21.2	0.055	0.150

Table 3: Values of $\lambda^2 J(J+1)$ for various isotopes.

2.3.3 Nuclear Form Factor

When the momentum transfer $q = (2M_T E_R)^{1/2}$, is such that the wavelength is no longer large compared to the nuclear radius, the effective cross-section begins to fall with increasing q. In the first Born (plane wave) approximation, the form factor is the Fourier transform of $\rho(r)$, the density distribution of the neutralino scatterers:

$$F(q) = \int \rho(r) \exp(i \cdot \vec{q} \cdot \vec{r}) d^3\vec{r} \tag{31}$$

The cross section σ_0 discussed in the former section is corrected by this form factor as $\sigma(q) = \sigma_0 F^2(q)$. A commonly used approximation for small momentum transfer is:

$$F^2(qr_n) = \exp(-(qr_n)^2/3). \tag{32}$$

where r_n is an effective nuclear radius and commonly used approximation is $r_n \sim A^{1/3}$fm or, $r_n \sim 0.89A^{1/3} + 0.30$fm[20]. The more precise studies have been done for spin-dependent and spin-independent interactions. For the spin-independent interactions, the form factor is written as:

$$F^2(qr_n) = \left[\frac{3j_1(qr_n)}{qr_n}\right]^2 \exp[-(qs)^2]. \tag{33}$$

where s $\sim$ 1fm is the nuclear skin thickness. Nuclear form factor as a function of recoil energy for spin-dependent and spin-independent cases are shown in Figure 6. For the spin-dependent interactions, if the single particle model is assumed, the zeros of the Bessel function is obtained from Eq.(31):

$$F^2(qr_n) = j_0^2(qr_n) \tag{34}$$

In the case of assuming odd group model, the form factor is approximated by the Bessel function partially filled with constant value:

$$F^2(qr_n) = \begin{cases} j_0^2(qr_n) & (qr_n < 2.55, qr_n > 4.5) \\ 0.047(\text{constant}) & (2.55 \leq qr_n \leq 4.5) \end{cases} \tag{35}$$

2.3.4 Counting Rate

As we shall mention in Section 3, our bolometer's absorber is LiF and we need to presume the recoil spectrum which will be obtained with the detector. We use the cross section and form factor corrections to the counting rate we discussed in Section 2.3.1. Neutralino-fluorine elastic scattering cross section is

$$\begin{aligned} \sigma_{\chi-F} &= \sigma_{\chi-p} \frac{\mu_F^2}{\mu_p^2} \frac{C_{\chi-F}^2}{C_{\chi-p}^2} \frac{\lambda^2 J(J+1)}{\lambda^2 J(J+1)} \\ &= 0.862 \cdot \sigma_{\chi-p} \frac{M_F}{M_p} \frac{M_p + M_\chi}{M_F + M_\chi} \end{aligned} \tag{36}$$

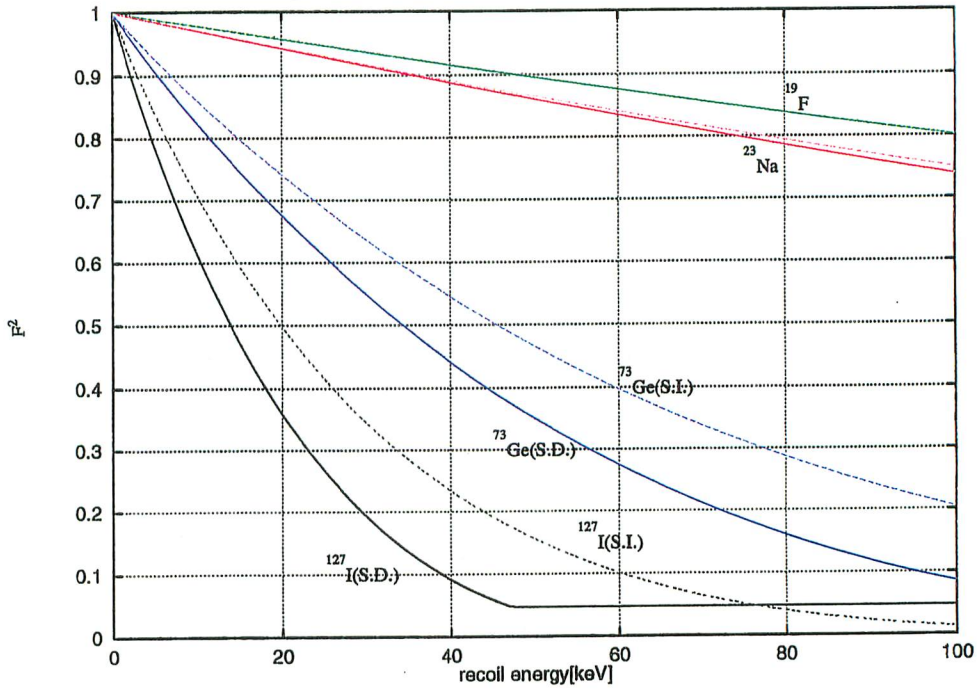

Figure 6: Nuclear form factor as a function of recoil energy for the spin-independent and spin-dependent interactions. Here, solid lines and dashed lines represent spin-dependent and spin-independent interaction form factors, respectively.

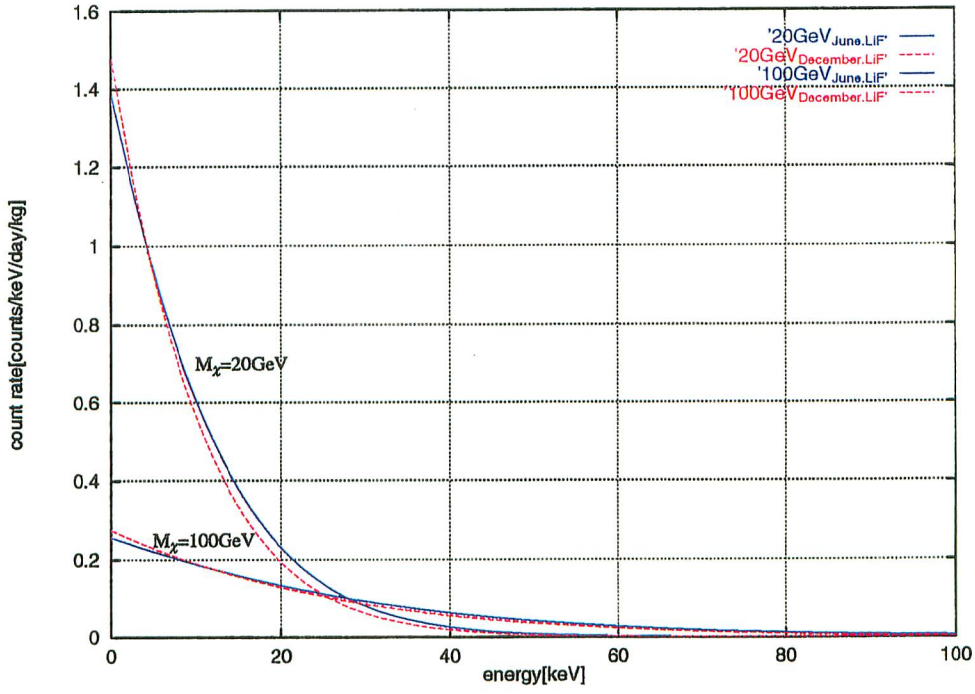

Figure 7: Expected recoil spectra of ^{19}F for M_χ=20 and 100GeV with seasonal modulation for both spectra. Here we take $\sigma_{\chi-p}$=0.1pb, v_0=230km s^{-1}, and $\rho_D = 0.4$GeV cm^{-3}.

where the odd-group model is assumed. Using Eq.(21), Eq.(27), Eq.(26), and Eq.(36), we can derive the recoil spectrum of ^{19}F. The calculated spectra are shown in Figure 7.

2.4 Accelerator Experiments for Neutralino Search

Neutralino search is also performed using the data from accelerator experiments. Here, we describe the recent result from OPAL collaboration based on Ref.[21]. Neutralino pairs ($\tilde{\chi}_1^0\tilde{\chi}_2^0$) can be produced by e^+e^- collision through an s-channel virtual Z, or by t-channel scalar electron (selectron, $\tilde{e}$) exchange. As we discussed in Section 2.3, neutralino-nucleus cross section is considered to be extremely small($\sim$ 0.1pb), therefore produced neutralinos are undetectable. The $\tilde{\chi}_2^0$ will decay into $\tilde{\chi}_1^0\nu\bar{\nu}$, $\tilde{\chi}_1^0\nu\bar{\nu}$, or $\tilde{\chi}_1^0 q\bar{q}$. Constrained Minimal Supersymmetric Standard Model(CMSSM) motivated by Grand Unification Theory(GUT) is often used for the analysis to simplify the physics interpretation. Figure 8 is

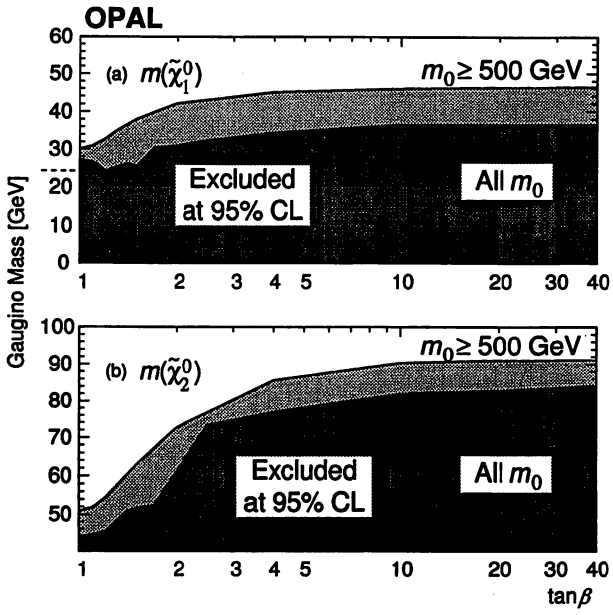

Figure 8: The 95% C.L. mass limit on (a) the lightest neutralino $\tilde{\chi}_1^0$ and (b) the second lightest neutralino $\tilde{\chi}_2^0$ as a function of $\tan\beta$ for $m_0 \geq 500$GeV in the framework of Constrained Minimal Supersymmetric Standard Model. The exclusion region for $m_0 \geq 500$GeV is shown by the light shaded area and the excluded region valid for all m_0 values by the dark shaded area. Here m_0 is the mass of the sfermions(SUSY partners of quarks and leptons[21] .

the obtained neutralino mass limit in the framework of CMSSM. The absolute lower mass for a certain parameter sets limit is 24.2GeV. However, searches for neutralino with mass lighter than 20 GeV are still needed because it is probable that GUT doesn't work. We still have little information on neutralino and measurements of the elastic scattering and accelerator examinations are both indispensable for the study of the neutralino.

3 Bolometer for Dark Matter Search

3.1 Bolometer

For the dark matter detection, some conventional detectors and other new ones are being used. In this section, we refer to ionization and scintillation detectors as conventional detectors. A cryogenic thermal detector (bolometer) measures the small temperature rise of the target material resulting from nuclear recoil. Bolometer, which is a rather new method for dark mater search, has some features as follows.

- Material Selection
  Most of insulators and superconductors have very small heat capacity at low temperature and can be used as an absorber. As we discussed in Section 2, some materials are sensitive to neutralino and we can choose one as the absorber.

- High Energy Resolution
  The average energy of thermal phonon is 2μeV at 20 mK. Therefore, for a given deposited energy bolometer senses much higher number of quanta than conventional detectors. In principle, much better energy resolution could be realized with a bolometer.

- Low Threshold
  The response of the conventional detectors to a nuclear recoil energy is different from that to an electron recoil. The detectors are generally calibrated with gamma ray sources, therefore, the quenching factor Q (ratio between the observed energy for a nuclear recoil and an electron of the same energy) has been measured for the proper energy evaluation. The quenching factors of conventional detectors are generally less than unity(see Table 4), that means the observed energy is less than the recoiled energy. On the other hand, the bolometer doesn't have quenching: i.e. $Q \sim 1$. Actually the quenching factor close to unity has been measured by Alessandrello[22].

- Slow Signal
  Since we observe the temperature rise of the target crystal, the time constant is governed by thermalization of the crystal and thermal conductivity to the refrigerator. Typical time constants are $\tau_{rise} = 5 \sim 20$ msec and $\tau_{decay} = 100 \sim 200$ msec, which are relatively slow compared with those of conventional detectors. In the early stage of the experiment, the count rate is still high and this slow signal is sometimes troublesome, however, the expected count rate of the dark matter is very low and this slow signal is not a problem for dark matter detection.

- Mass Limit
  For the rare event search, a large detector mass is required. A large mass

Detector	Nucleus	Q
NaI(Tl)[23]	Na	0.30
	I	0.08
CaF_2(Eu)[24]	Ca	0.08
	F	0.12
CaF_2(Eu)[25]	Ca	0.09
	F	0.11
Ge[26]	Ge	0.25
Si[27]	Si	0.30

Table 4: Measured quenching factors for semiconductor and scintillation detectors.

bolometer, however, leads to small signal to noise ratio because the heat capacity of the absorber is proportional to the mass. With an array of some small pieces of bolometer, enough mass can be obtained.

- Operation Difficulties
  Since the bolometer experiment involves cryogenic technique, the operation is rather difficult compared with the operation of conventional detectors. The cooling procedure takes at least one week before the measurement. Sometimes we suffer from unexpected cryogenic problems.

3.2 Neutron Transmutation Doped Thermistors

The recoil energy caused by the neutralino interaction is less than order of several tens of keV. In order to realize low threshold, we have fabricated very sensitive phonon sensor[28]. The sensor is a heavily doped germanium thermistor manufactured by neutron transmuted doping (NTD) method. NTD method provides uniform dopants concentration in the germanium. The schematic drawing of the fabricated NTD thermistor is shown in Figure 9 and the RT curves of NTD thermistors used for the dark matter search experiments are shown in Figure 10. The good reproductivity of the thermistor is seen in Figure 10 and this feature gives a significant advantage in constructing a multiple array of the bolometers.

3.3 Dark Matter Search Experiment in the Surface Laboratory

With a 21-g LiF bolometer, we made a test running in the surface laboratory in the Hongo campus of the University of Tokyo. Details are described in Ref.

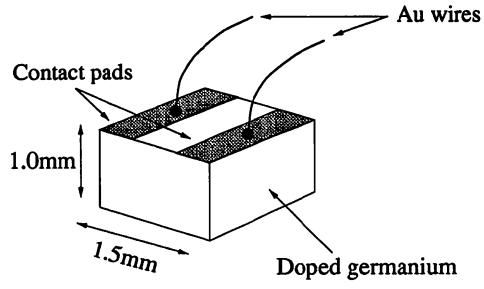

Figure 9: Schematic drawing of the fabricated NTD thermistor. The Au wires are 50 μm diameter.[28]

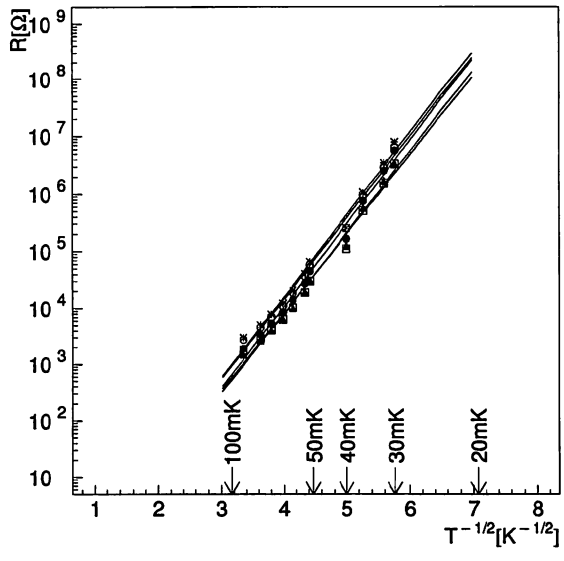

Figure 10: RT curves of five NTD thermistors used for the surface and underground experiments.[28]

[29]. The shieldings for the surface test running is shown in Figure 11. The shielding consists of 10cm thick lead layer and the coverage is 96%.

We have obtained the spectrum shown in Figure 12. From the obtained energy spectrum, we have derived an exclusion plot for the spin-dependently interacting WIMP-proton cross section(Fig. 13). Limits from other experiments are shown in Figure 33.

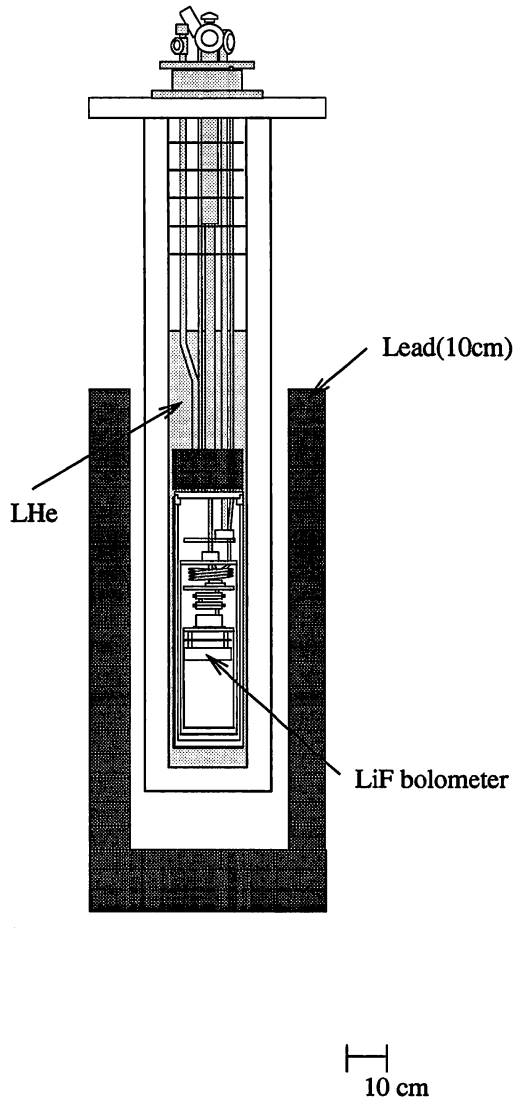

Figure 11: Schematic view of the passive shielding for the surface measurement.

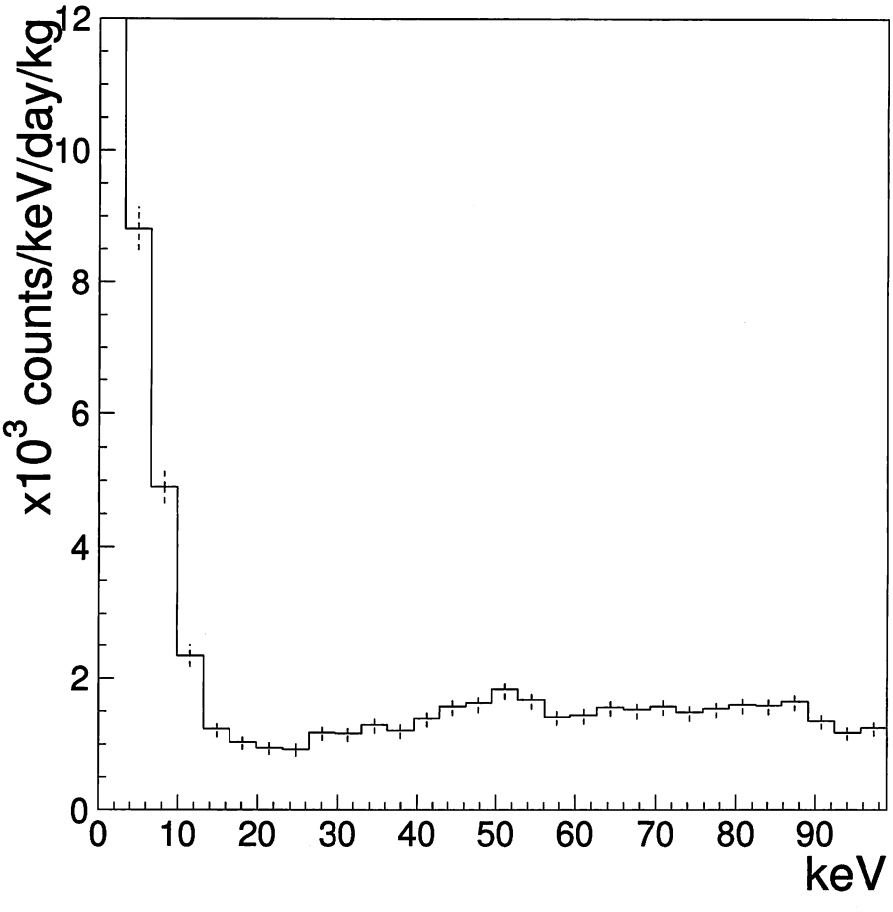

Figure 12: Background spectrum obtained with a LiF bolometer in the surface laboratory. An exposure is 21g × 1.19 days. The detector is surrounded by 10cm-thick lead shielding.[29]

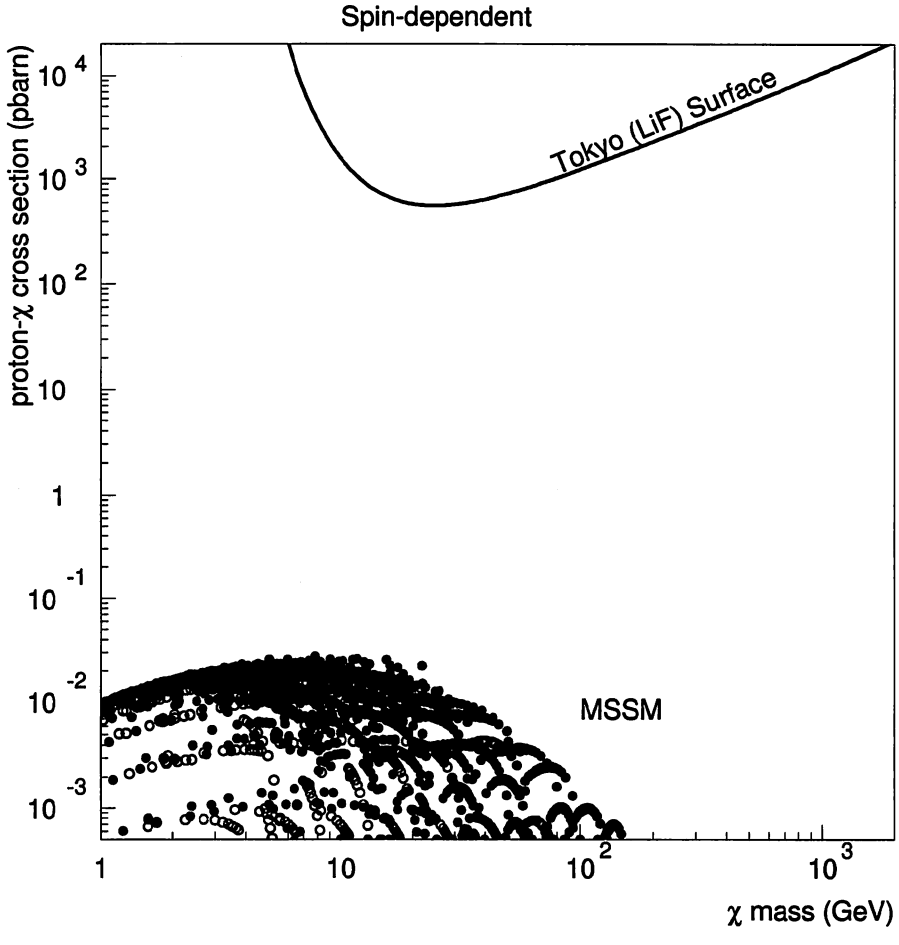

Figure 13: Excusion plot derived from the background spectrum shown in Figure 12 for spin-dependent interacting WIMP mass. The scatter plot predicted in MSSM are also shown.[29]

4 Nokogiriyama Underground Cell(Background Reduction I)

We have successfully developed a LiF bolometer and performed the test running in the surface laboratory. We confirmed that the detector is working as expected and learned that we need to reduce the background by more than five orders of magnitude(Fig. 13).

The background reduction is achieved by:

- Going deeper underground
- Employing appropriate shieldings

We can reduce the muon flux by going deeper underground, and the ambient gamma, beta rays, and neutrons by employing appropriate shieldings. In this section and the following one, an attempt to reduce the background of our bolometer is described.

4.1 Nokogiriyama Underground Cell

Nokogiriyama underground cell is located at the foot of a hill near Mt. Nokogiriyama in Futtsu city, Chiba prefecture. It is about 60km south from Tokyo. The cell is relatively easy to access from Tokyo and is a suitable place to perform development and measurement simultaneously. Access to the cell from the hillside can be made through a 10m tunnel. The cell is situated perpendicular to this tunnel. Our experimental space is 2–3 m high, 2.7m wide, and 11m long. Air is forced to flow with an exhaust fan and is dehumidified .

4.2 Muon Flux Measurement in Nokogiriyama Underground Cell

Most of dark matter search experiments are being performed at deep underground sites(Fig. 14), because muon flux is reduced by an order of three with some hundred meter water equivalent(m.w.e)(Fig. 15).

At shallow depth site like Nokogiriyama underground cell, muon's ionization, fast neutrons produced in lead shielding by muons, muon-induced electron-photon showers are thought to be serious background for dark matter search. We measured the muon flux in Nokogiriyama underground cell beforehand in order to design an appropriate veto system. We could also estimate the water equivalent depth of the cell.

4.2.1 Measurement Set-up

A plastic scintillator (250mm × 250mm × 20mm^t) with a light guide and a photomultiplier tube (R329-01,Hamamatsu Photonics K. K.) was used for the

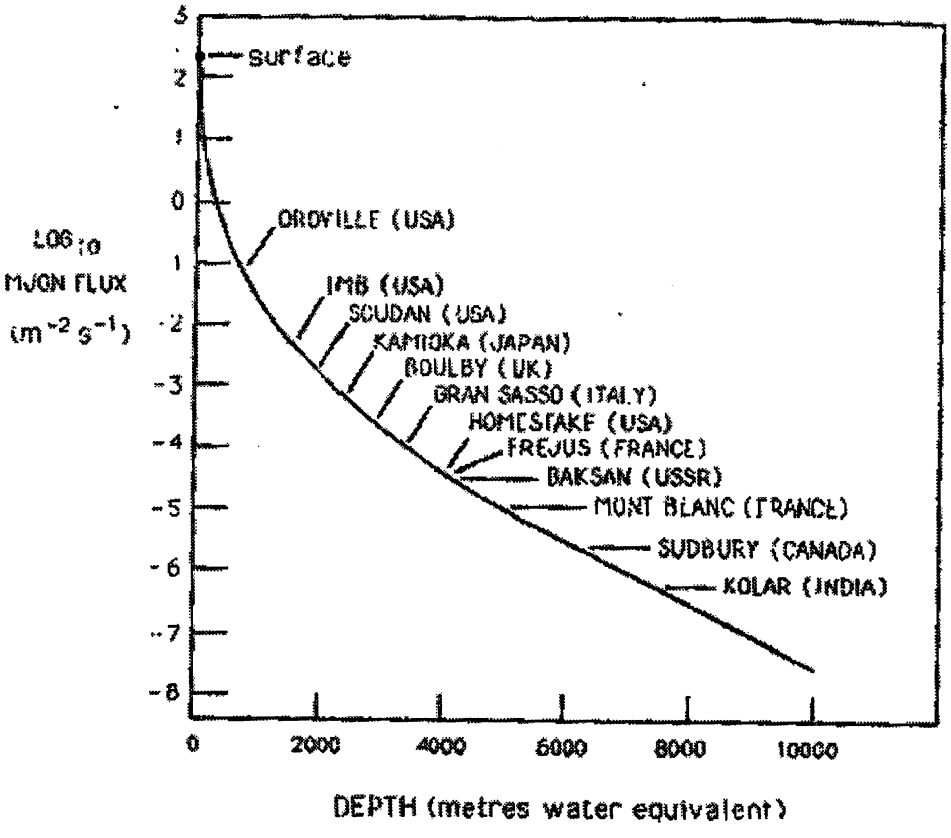

Figure 14: Some underground physics site[17]. Dark matte search experiments are performed in Boulby(UK) and Gran Sasso(DAMA and BPRS).

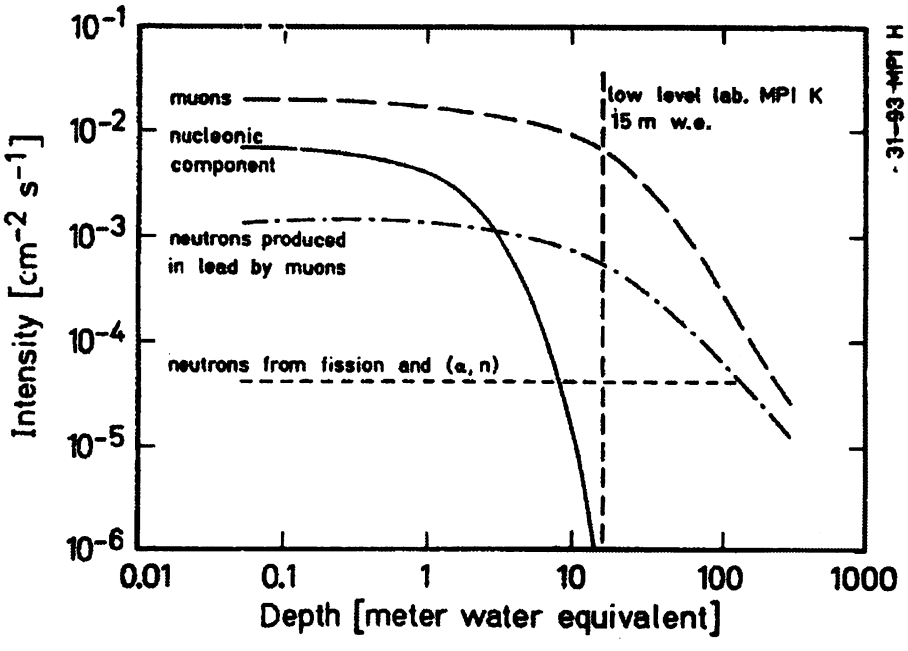

Figure 15: Flux of secondary and tertiary cosmic rays relevant to cosmic ray-induced background of shielded detectors and of the neutrons from primordial radionuclides[30].

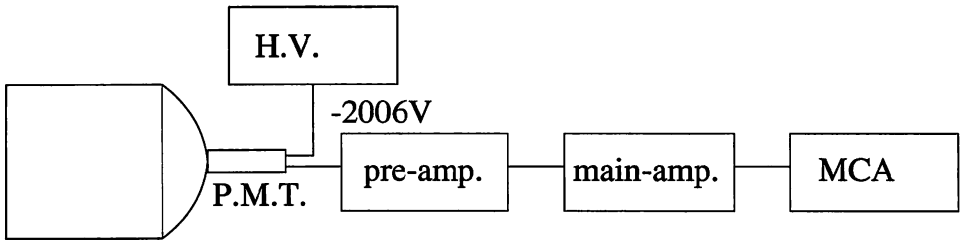

Figure 16: Schematic diagram of the muon flux measurement.

place	muon flux[$m^{-2}s^{-1}$]
Hongo	1.1×10^2
Nokogiriyama	3.4×10

Table 5: Muon flux measured in Nokogiriyama underground cell and in the surface laboratory.

measurement. High voltage (-2006V) was supplied by a Cambera high voltage supplier. The set-up is illustrated in Figure 16.

In order to compare the muon flux in Nokogiriyama underground cell with that in the surface, the measurement was performed both in Nokogiriyama underground cell and in the Hongo campus of the University of Tokyo.

4.2.2 Result

The obtained spectra are shown in Figure 17. It is seen that the integrated count rate of the minimum ionization peak (> 2.2MeV) measured in Nokogiriyama underground cell is about one third of that in the surface, which infers that the depth of overburden is at least 10 m.w.e. The fluxes calculated from the spectra are shown in Table 5. Figure 15 indicates that in a shallow depth site like Nokogiriyama underground cell, although nucleonic component is sufficiently reduced, we will suffer from the background due to cosmic ray muons.

4.3 Gamma Ray Flux Measurement in Nokogiriyama Underground Cell

Gamma rays will be the dominant background source in any laboratories without any shieldings of high-Z materials. In order to design an appropriate shield-

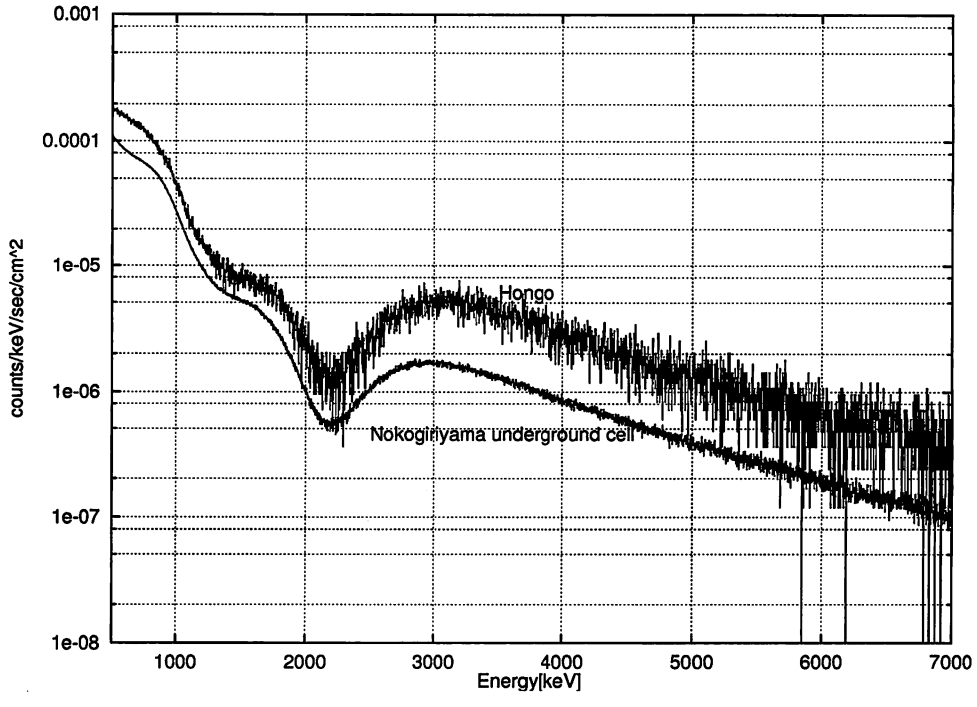

Figure 17: Obtained spectra with a plastic scintillator. The peak due to the minimum ionization by muon, Compton edges by ^{40}K, and ^{208}Tl are clearly seen. The live times are 5320 sec and 451470 sec for measurement in Hongo and Nokogiriyama underground cell respectively.

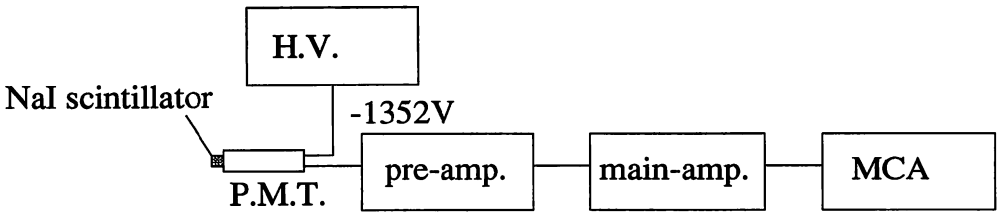

Figure 18: Schematic diagram of the gamma ray flux measurement.

ings for the underground experiments, we measured gamma ray flux in Nokogiriyama underground cell with an NaI scintillator.

4.3.1 Measurement Set-up

An NaI scintillator of 1" diameter and 1" thickness was attached to a photomultiplier tube (R594,Hamamatsu Photonics K. K.) with silicone grease and used for the measurement. High voltage(-1352V) was supplied by a Repic RPH-030 high voltage supplier. The set-up is illustrated in Figure 18. The measurement was performed in Nokogiriyama underground cell and in the Hongo campus of the University of Tokyo for comparison. The measurement was also performed in a 10cm thickness of 4π lead shielding in order to estimate the radio activity of the detector.

4.3.2 Result

The obtained spectra are shown in Figure 19. The peak due to photoelectric absorption from ^{40}K, its Compton edge, and photoelectric peak by ^{208}Tl(2.614 MeV gamma ray) are clearly seen. The count rates integrated from 100keV to 2.8MeV are shown in Table 6. The gamma ray flux in the Nokogiriyama underground cell were found to be 1.20 times larger than that measured in the Hongo campus. Gamma ray flux in the Hongo campus has been measured with HPGe detector and was known to be 1.5cm^{-2}s^{-1}(Section B,Fig. 56).

Using that result, we can estimate the gamma ray flux in the Nokogiriyama underground cell that is also shown in Table 6. The calculation is based on Eq.(37).

$$\Phi_{\mathrm{Noko}} = \Phi_{\mathrm{Hongo}} \cdot \frac{\phi_{\mathrm{noko}} - \phi_{\mathrm{Background}}}{\phi_{\mathrm{hongo}} - \phi_{\mathrm{Background}}} \tag{37}$$

Where Φ is the gamma ray flux and ϕ is the count rate obtained with the NaI detector. We calculated the ratio of the gamma ray fluxes measured in Nokogiriyama underground cell to that measured in Hongo. The result is shown in Figure 20. It is seen that the lower energy gamma ray flux is 1.5 times higher

place	count rate[cps]	gamma ray flux[$cm^{-2}s^{-1}$]
Hongo	13.6	1.5
Nokogiriyama	20.2	2.2
Background	1.06	7.7×10^{-2}

Table 6: Gamma ray flux measured in Nokogiriyama underground cell, Hongo and inside 10cm-thick lead shielding(Hongo). The gamma ray flux in the Hongo campus was measured with HPGe detector and was used for the estimation of the flux in Nokogiriyama underground cell and of the background. Count rate and gamma rat flux are integral of the spectrum between 100 keV and 2.8 MeV.

in Nokogiriyama underground cell than in Hongo. There exists large amount of sand outside of the Nokogiriyama underground cell, while the room in the Hongo campus has concrete wall of $\sim$ 10cm thick. Sand and concrete both contain ^{40}K, U, and Th, the amount of these contaminants determines the ambient gamma ray flux. The measurement result implies the necessity of more effective shieldings than those in Hongo.

4.4 Neutron Flux Measurement in Nokogiriyama underground Cell

Neutrons produced in high-Z shielding materials by cosmic ray muons can be one of the dominant background sources. Neutrons are also produced in the surrounding rocks and materials employed to construct the detector system from spontaneous fission of ^{238}U and from (α, n) reactions. At a shallow depth site like Nokogiriyama underground cell, it is reported that the neutron flux from cosmic ray muon is larger than that from fission and (α, n) approximately by an order of two(Fig. 15[30]).

Neutrons produced in these procedures become background by the following ways.

- A neutron scatters off a nucleus in the detector to cause a nuclear recoil.
- A neutron scatters inelastically off a nucleus with γ emission.
- ^{6}Li captures a neutron to create tritium:i.e.

$$\begin{aligned} {}^6\mathrm{Li}(7.5\%) + \mathrm{n} &\rightarrow {}^3\mathrm{H} + \alpha \ (\mathrm{Q} = 4.78\mathrm{MeV}) \\ {}^3\mathrm{H} &\rightarrow {}^3\mathrm{He} + \mathrm{e}^- + \overline{\nu}_\mathrm{e} \ (\mathrm{T}_{1/2} = 12.3\mathrm{y}, \mathrm{Q}_\beta = 18.6\mathrm{keV})(38) \end{aligned}$$

The cross section of the neutron capture reaction is large(942barns)[31] and this will be an important background, for the Q-value is just above our detector's threshold and we are searching for very low rate signals.

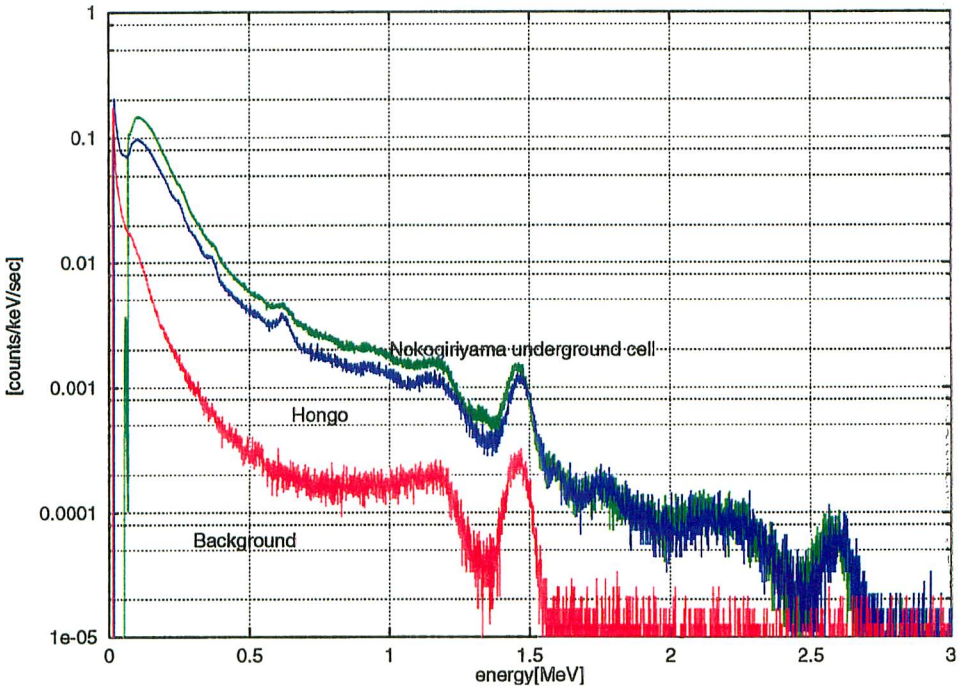

Figure 19: Obtained gamma ray spectra. The peak from ^{40}K(1.46MeV) and ^{208}Tl(2.61MeV) are clearly seen. In the spectrum measured in Hongo, the peak from ^{214}Bi(0.61MeV) is also seen.

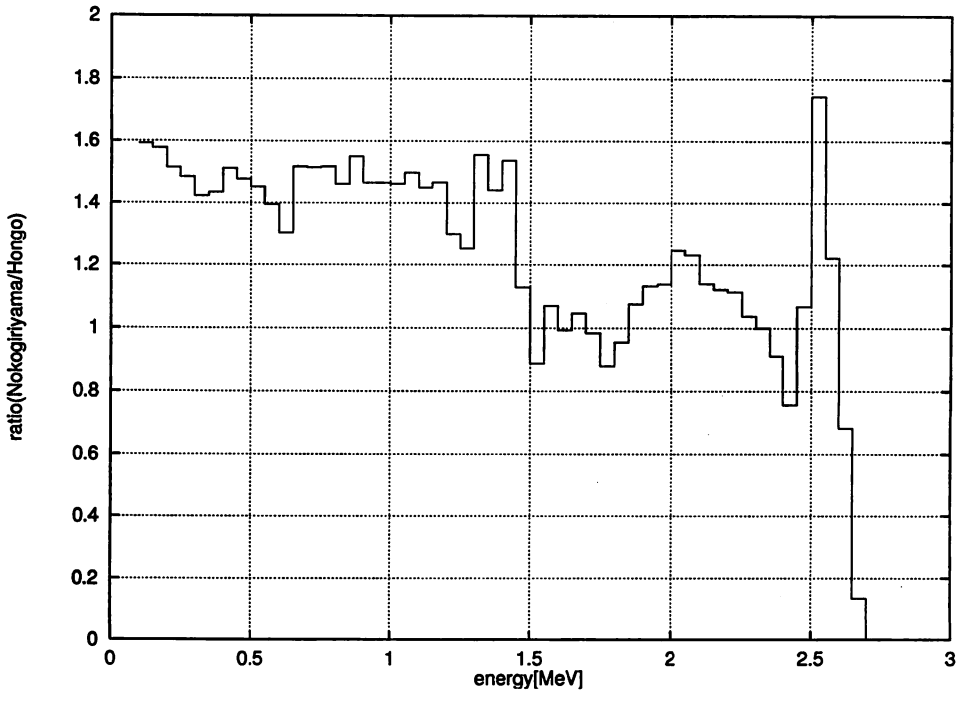

Figure 20: Gamma ray flux ratio measured in Nokogiriyama underground cell to that measured in the Hongo campus. The background flux is subtracted from each flux and the fluxes are compared.

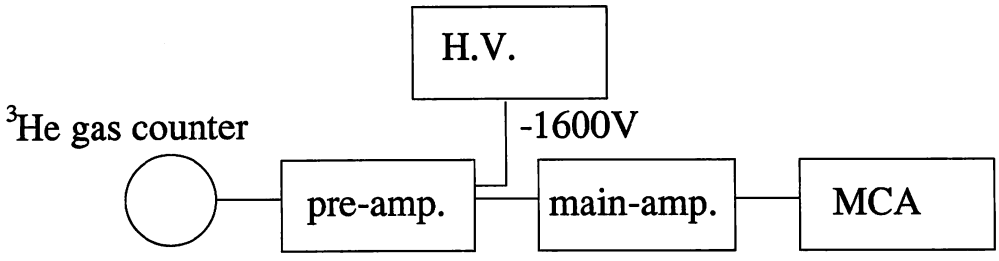

Figure 21: Schematic diagram of the neutron flux measurement.

4.4.1 Measurement Set-up

The experimental set-up used in the neutron flux measurement is shown in Figure 21. The detector is a 2-inch-radius spherical gas counter which contains 10 atm of ^{3}He. The reaction to detect the neutron is thermal (low energy) neutron capture: i.e.

$$^3\mathrm{He} + \mathrm{n} \rightarrow {}^3\mathrm{H} + \mathrm{p}. \qquad \mathrm{Q} = 765\mathrm{keV} \tag{39}$$

The cross section of this reaction is 5330 barns and has higher values at thermal range.[32] The response of this detector is precisely studied by Y. Uwamino et al.(Fig 22),[33]. For the estimation of the flux of fast (high energy) neutrons, the detector is covered with a 5.1cm thickness of polyethylene or a 0.5mm thickness of cadmium. Polyethylene moderates fast neutrons and cadmium absorbs thermal neutrons. The thermal neutron capture cross section of Cd is 2530 barns. Hereafter, we refer to neutrons with energies below and above 5eV thermal neutrons and fast neutrons, respectively. The obtained spectrum of the measurement is shown in Figure 23. The peak in the spectrum is formed by absorption of the kinetic energy of the tritium and proton in the ^{3}He gas. Information on the energy of neutrons are lost and the shape of the spectrum is only due to the detector's size, shape, and pressure of the ^{3}He gas. As the neutrons produced in high-Z materials are thought to be the dominant fast neutron source in the Nokogiriyama underground cell, the neutron flux in the Nokogiriyama underground cell was measured inside and outside of the radiation shieldings employed in this dark matter search experiment. The schematic view of the shieldings is shown in Figure 28. The results are listed in Table 7. As the thermal neutron flux inside of the shieldings was below the sensitivity of the ^{3}He counter, it was measured by using the thermal neutron capture reaction of ^{6}Li in the bolometer[34](Eq. (38)).

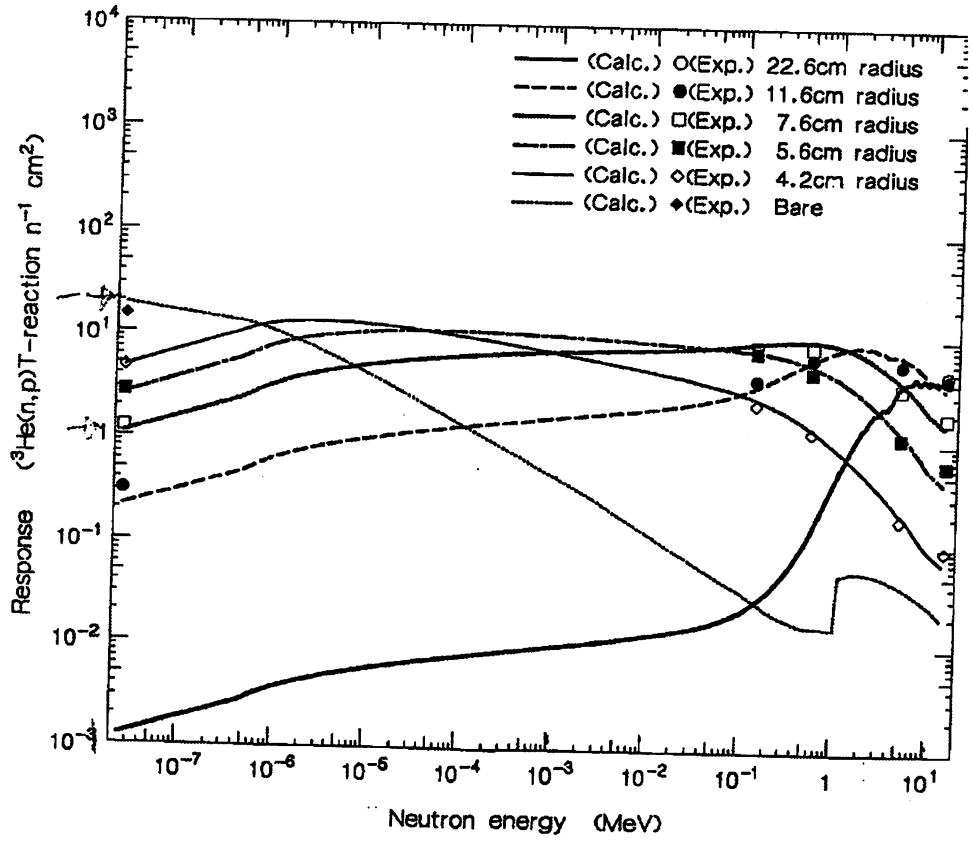

Figure 22: Measured and calculated response of the ^{3}He neutron detector[33].

	thermal[$cm^{-2}s^{-1}$]	fast[$cm^{-2}sec^{-1}$]
Hongo	1.9×10^{-3}	1.2×10^{-2}
Nokogiriyama(outside of the shieldings)	9.4×10^{-5}	4.9×10^{-4}
Nokogiriyama(inside of the shieldings)	1.9×10^{-5}	3.2×10^{-3}

Table 7: Measured neutron flux in the surface laboratory and Nokogiriyama underground cell. The thermal neutron flux inside of the shieldings is measured with the LiF bolometer.

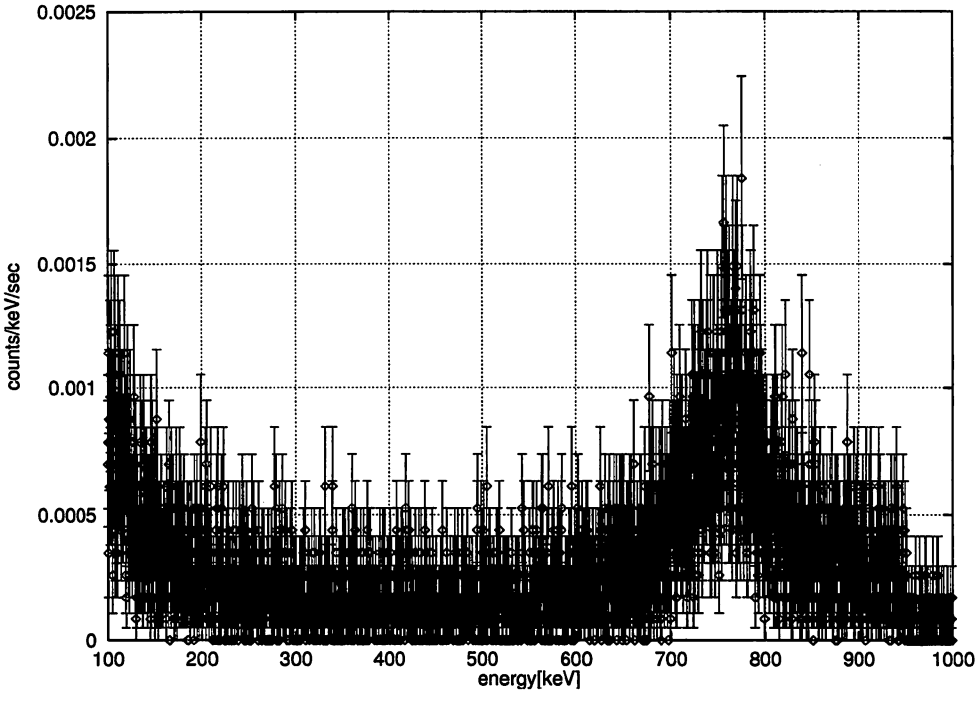

Figure 23: Obtained spectrum with the ^{3}He counter in Nokogiriyama underground cell. Information on the neutron energy is lost.

4.4.2 Result

The ambient neutron flux in Nokogiriyama underground cell is reduced by a factor of $20 \sim 30$ compared with the flux in the surface. With the polyethylene and boric acid shieldings, thermal neutron is further reduced by a factor of five. On the other hand, the fast neutron are produced in the high-Z materials and the flux is larger in the shieldings by a factor of six. This result is well consistent with the neutron flux shown in Figure 15.

Although the neutron flux in Nokogiriyama underground cell is smaller than that in the surface, the amount of tritium created in the LiF crystal by thermal neutron capture(Eq.(38)) increases since the fabrication of the crystal. To avoid the reaction, the crystals are kept within a shieldings of 30cm-thick polyethylene and 1mm-thick cadmium in the Nokogiriyama underground cell.

4.5 Veto System

As we learned from the muon flux measurement(Sec. 4.2), Nokogiriyama underground cell is not a very deep underground laboratory and an appropriate veto system is indispensable to avoid cosmic ray muon induced background. The schematic view of the designed veto system is shown in Fig. 24 along with the shieldings and the refrigerator.

The veto system consists of twenty sheets of BC-412 plastic scintillators by BICRON with a thickness of 20mm and a width of 300 mm. The scintillation light is seen from one end of the scintillator through an acrylic light guide by photomultiplier tube H6410(Hamamatsu Photonics K. K.). The light attenuation of the plastic scintillator was checked in advance and the position dependence of the light yields was found to be within $\pm 10\%$, that is enough to discriminate muon's inonizatio from ambient gamma rays. We divided the veto system into three areas for the estimation of the coverage: i.e. area A consists of three identical($300\text{mm} \times 1500\text{mm} \times 20\text{mm}^t$) scintillators which are mounted above the refrigerator in flat, area B consists of five scintillators which hung vertically below area A, and area C consists of twelve identical($300\text{mm} \times 2000\text{mm} \times 20\text{m}^t$) scintillators which surround the lead passive shielding. Because of the geometrical restriction, we didn't set any scintillators under the shieldings. In the calculation of the geometrical coverage, we assume muon's zenith angle distribution to be $\cos^2\theta$ and the defect of the area under the shieldings is not counted. The coverages of the three areas are shown in Table 8. The geometrical coverage is estimated to be $\sim 90\%$. The incompleteness of the geometrical coverage is due to the drain of the vacuum tubes and the tube of the helium liquefier.

The block diagram used for the veto system is shown in Fig. 25. The pulse from each plastic scintillator is fed into three 8-channel discriminators. The output from the discriminator is connected to 32-channel multiplicity logic module where multiplicity is set to one. The logic pulse from the multiplicity logic module is fed to a gate generator. The output of the gate generator is then

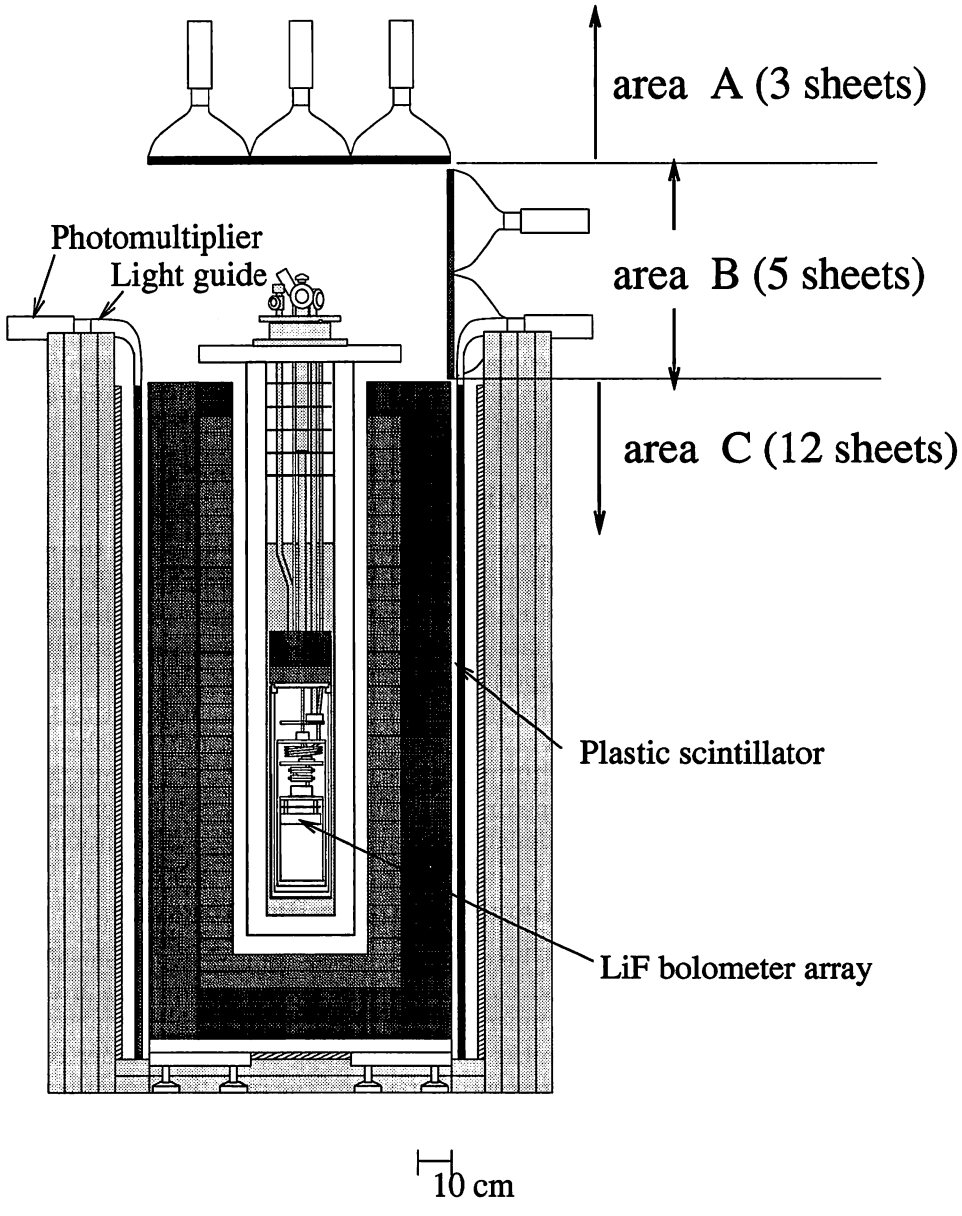

Figure 24: Schematic view of the veto system.

area	coverage([m^2]/[m^2])	effective solid angle
A	83%(1.26/1.52)	11%
B	56%(1.74/3.1)	10%
C	100%(7.2/7.2)	79%
total	90%	

Table 8: Geometrical coverage of the plastic scintillators. Effective solid angle is defined as solid angle (seen from the detector)[%]× muon's zenith angle distribution where $\cos^2\theta$ is assumed.

fed through a saw wave generator into a 16-bit waveform digitizer VXI module. By using a saw wave generator, we can achieve better time resolution than the sampling rate of the digitizer(1kHz for veto).

4.6 Radiation Shieldings

In this section, the configuration of the passive shieldings and the material selection is described. Appropriate material for the shielding is different according to the background source: i.e. high-Z material for gamma and beta ray absorption, H-rich material for fast neutron moderation, and some specific material for thermal neutron absorption.

The background without any shieldings is easily estimated using the result of the measument of gamma ray and neutron fluxes. Estimated backgrounds without any shieldings are $\sim 10^4$ counts/keV/kg/day and ~ 1 counts/keV/kg/day due to gamma rays and neutrons, respectively. This estimation suggests that the shieldings should be designed mainly for gamma ray absorption.

4.6.1 Shieldings for Gamma and Beta Ray Absorption

For ambient gamma and beta ray absorption, we designed shieldings which consist of 15cm-thick lead outer layer and 10cm-thick oxygen free high conductivity(OFHC) copper inner layer. Lead shielding effectively absorbs gamma and beta rays from the rocks and surrounding apparatus. Inner copper layer shielding absorbs the fluorescence X-rays and the radiation from the radioactive contamination in lead.

The radioactive contamination in lead can be categorized in two types:

- K, U-chain, and Th-chain isotopes
  K, U-chain, and Th-chain isotopes are important background sources which are contained in most materials. In construction of the dilution refrigerator, we chose low-background materials[36]. We again selected the materials for the shieldings using the low-background HPGe detector.

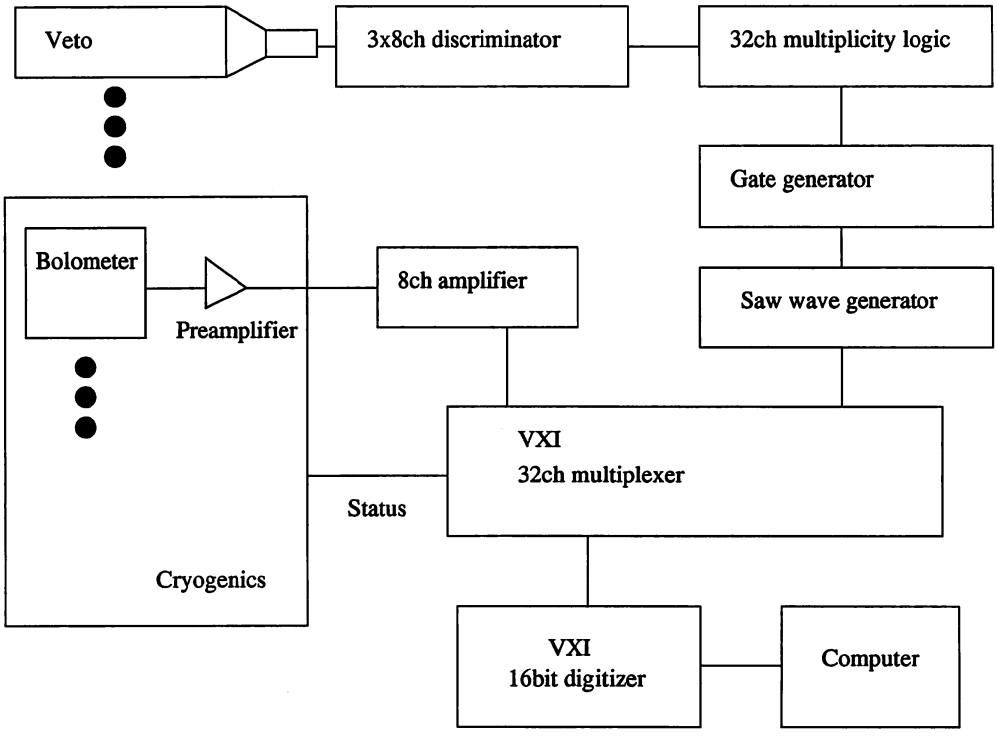

Figure 25: Schematic diagram of the veto system along with the bolometer data acquisition.

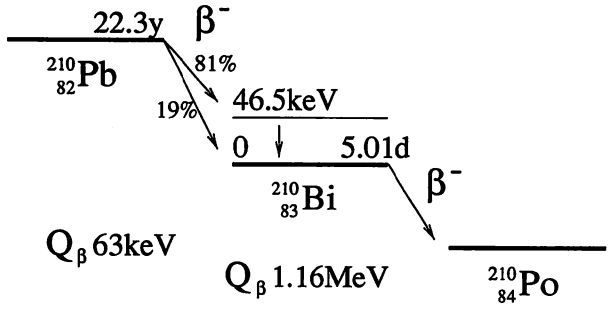

Figure 26: Decay scheme of ^{210}Pb.

We checked three types of lead and found that their concentration of these contamination are below the detection limit for all of the three samples. The results are listed in Table 9. As for lead C, which was selected as the material for the underground experiment, concentration of K contamination was also measured by mass analysis method. The concentration of K contamination was again below the detection limit.

- Radioactive lead isotope ^{210}Pb
  ^{210}Pb is background source peculiar to lead and is troublesome because it cannot be removed by chemical purification and is long-lived($T_{1/2}$ = 22.3yr). The decay scheme of ^{210}Pb is shown in Figure 26. Because of the large Q value of the bata decay of ^{210}Bi (1.16MeV), the bremsstrahlung radiation can be one of the most important background sources. We can estimate the concentration of ^{210}Pb contamination with HPGe detector by measuring the 46.5 keV peak from ^{210}Pb decay. The obtained spectra of the three samples are shown in Figure 27. The calculated concentrations of the ^{210}Pb contamination are listed in Table 9.

The result of the measurements clearly shows the radioactive contamination of the three samples. Peak from ^{210}Pb(46.5keV) is clearly seen in the spectrum of lead A, while the spectrum of lead C doesn't show any peak there. In the spectrum of lead A, a broad continuum due to the beta decay of ^{210}Bi is seen around 150 keV. We can further know the radioactive contamination by comparing the Pb X-rays around 80 keV, as the X rays are thought to be generated by the gamma and beta rays from the redioactive contamination within the samples. It is apparent that lead C contains least radioactive contamination. Therefore, we chose lead C as the material for the shieldings.

Copper is free from radioactive isotope which can be background source, so we selected the OFHC copper by checking the K,U, and Th contamination with the HPGe detector. Three samples were checked, and no contamination was

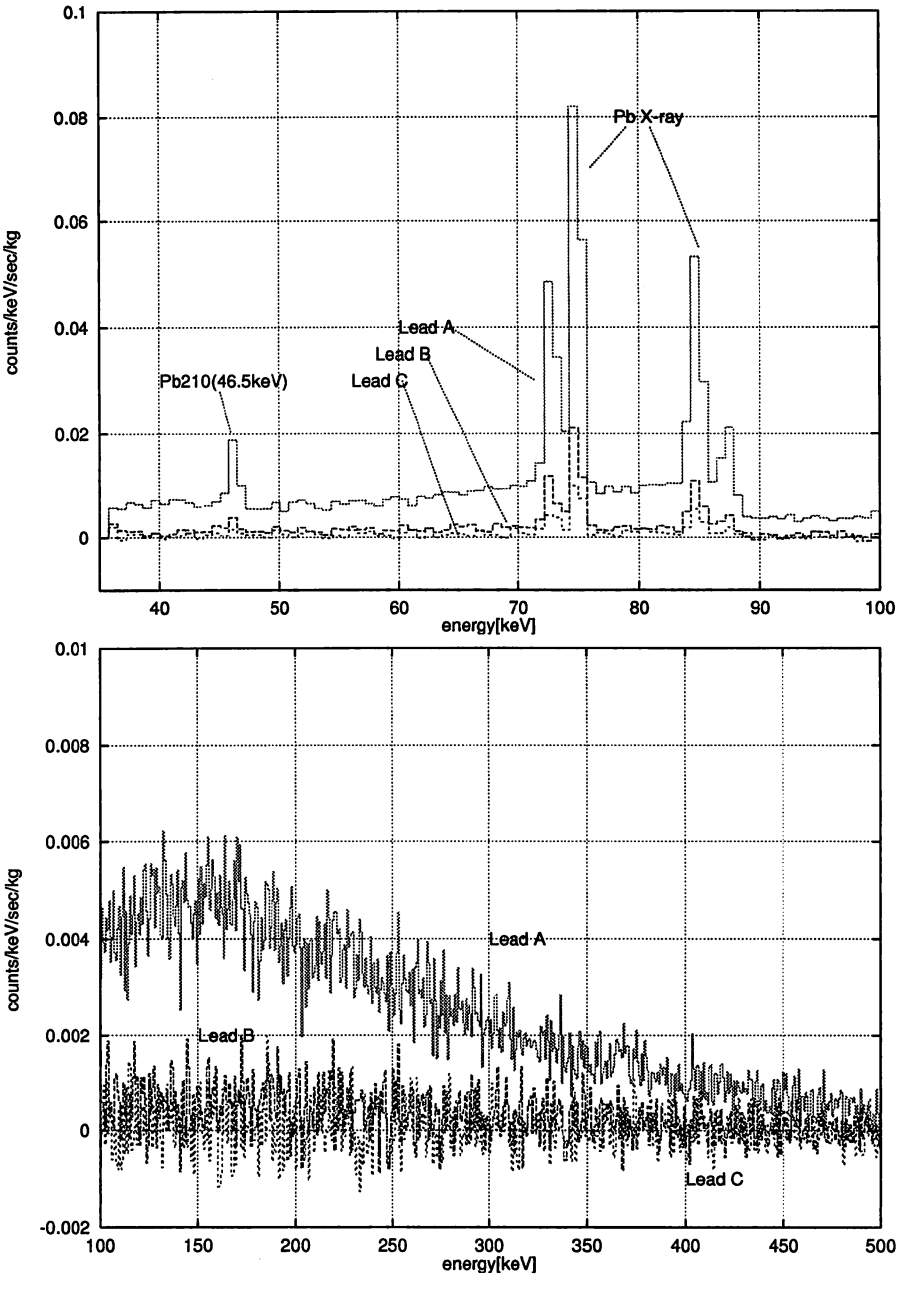

Figure 27: Obtained spectra of three lead samples. In the spectrum of lead A, a large peak at 46.5 keV and the broad continuum around 150keV are clearly seen. The broad continuum is due to the beta decay of ^{210}Bi. In all of the three spectra, peaks from lead K X-rays(72.8 keV, 75.0 keV, 84.9 keV and 88.0 keV) are seen.

	U[ppb]	Th[ppb]	K[ppm]	^{210}Pb[pCi/g]
Lead A	< 2.2	< 39	< 12	0.58
Lead B	< 2.5	< 33	< 10	0.10
Lead C	< 2.1	< 30	< 8.2	< 0.05
Lead C(mass analysis)	0.6	1.5	< 1	-

Table 9: Concentration of radioactive contamination in lead samples. The above three are measured using the low-background HPGe detector. As for lead C, contamination of U and Th was analyzed by Japan Energy Analytical Research Center, contamination of K was analyzed by Kawasaki Steel Sechno-Research Corporation.

	U[ppb]	Th[ppb]	K[ppm]
OFC A	< 1.6	< 1.6	< 0.9
OFC B	< 1.6	< 0.7	< 0.6
OFC C	< 0.7	< 0.6	< 0.8
OFC C (mass analysis)	< 0.1	0.6	< 1

Table 10: Concentration of radioactive contamination in copper sample. The above three are measured using the low-background HPGe detector. As for OFC C, contamination of U and Th was analyzed by Japan Energy Analytical Research Center, contamination of K was analyzed by Kawasaki Steel Techno-Research Corporation.

detected. The upper limits of the concentration of these radioactive contaminants are listed in Table 10. As for the material employed for the underground experiment(copper C), the concentrations of the contamination were measured by mass analysis method.

We decided the thickness of the lead and copper layers by simulation. Figure 29 shows how ambient gamma rays are attenuated by various thickness of lead layer. With 15cm-thick lead, the ambient gamma ray flux is reduced by 4$\sim$5 orders of magnitude. We simulated the bremsstrahlung effects using the result of the measurements of radioactive contamination in lead and found that with 10cm copper layer, the background will be less than 0.5 counts/keV/day/kg.

We employed 15cm and 10cm as the thickness of outer lead layer and inner copper layer, respectively. Pictures of the passive shieldings are shown in Figure 30.

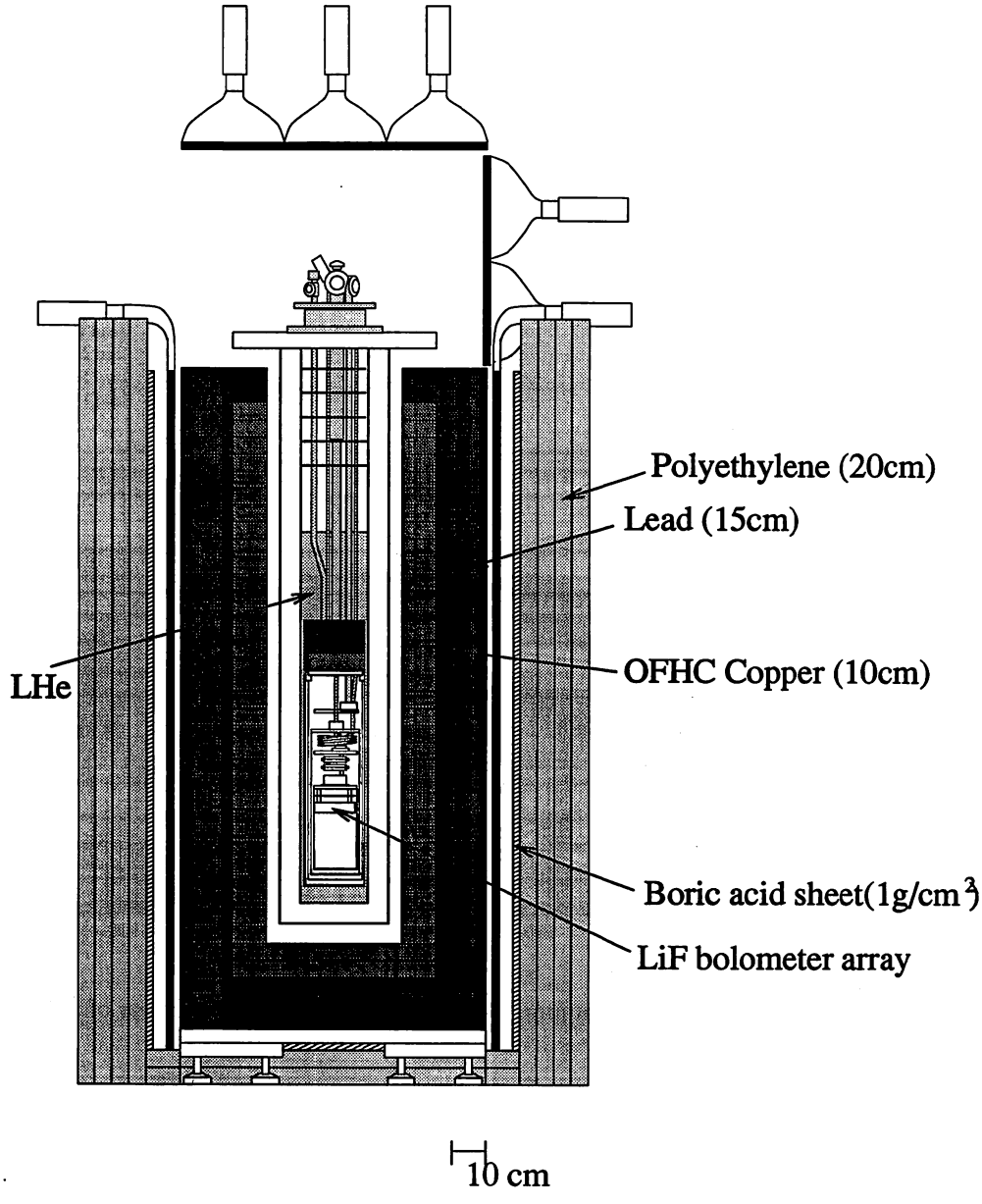

Figure 28: Schematic view of the passive shieldings.

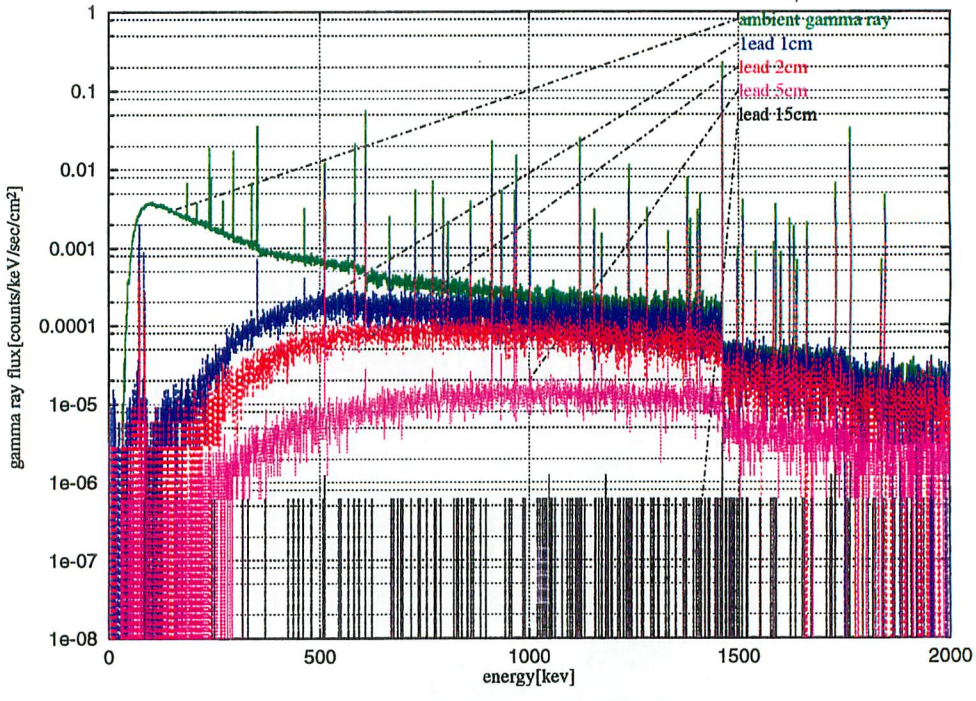

Figure 29: Simulated gamma ray spectra with various thickness of lead layer.

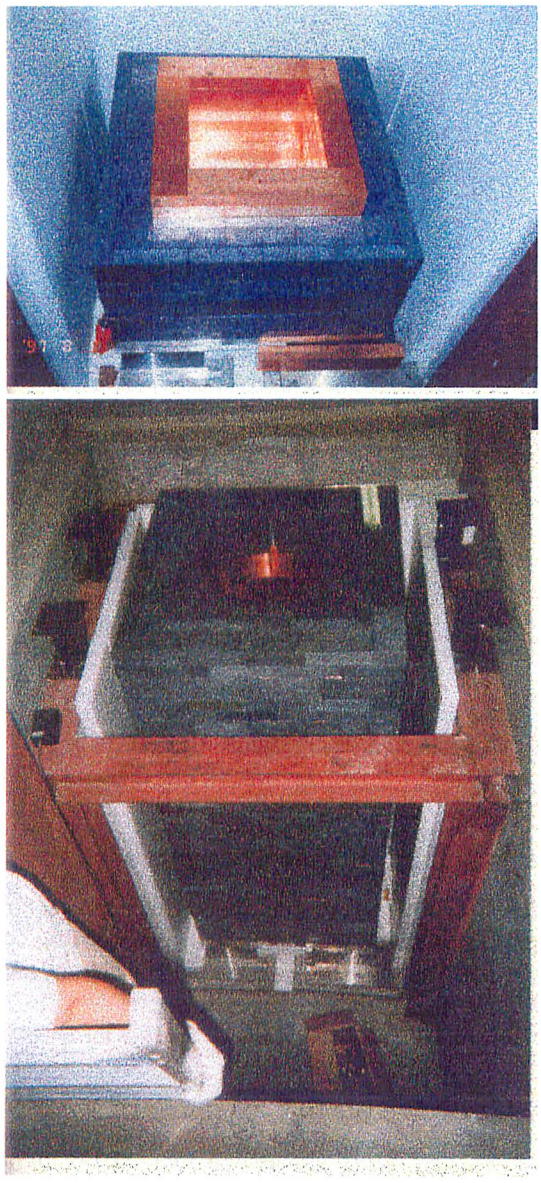

Figure 30: Pictures of the passive shieldings.

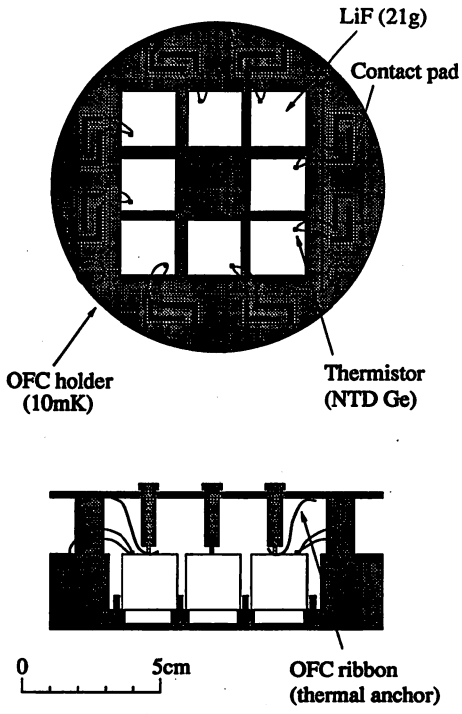

Figure 31: Schematic drawing of the bolometer array used for the first underground experiment. Each LiF crystal is 21g[34].

4.6.2 Shieldings for Neutron Absorption

We designed neutron absorption shieldings which consists of 20cm-thick polyethylene layer and 1g/cm^2-thick boric acid layer. According to Ref.[35], this shielding reduces the neutron flux by a factor of $2 \sim 5$ Polyethylene moderates fast neutrons and boric acid captures thermal neutrons. The thermal neutron capture cross section of ^{10}B(natural abundance 19.9%) is 3838 barns.

4.7 First Underground Experiment

With a bolometer array which consists of 8 × 21g LiF bolometers, the veto system, and the passive shieldings, we performed the first underground experiment in Nokogiriyama underground cell. Schematic drawing of the bolometer array is shown in Figure 31. Details are described in Ref.[34].

We have obtained the spectrum shown in Figure 32 and have derived an exclusion plot for the spin-dependently interacting WIMP-proton cross sec-

tion(Fig. 33). In this experiment, we have set the most stringent limit for the cross section of spin-dependently interacting neutralino with a mass lighter than 5 GeV.

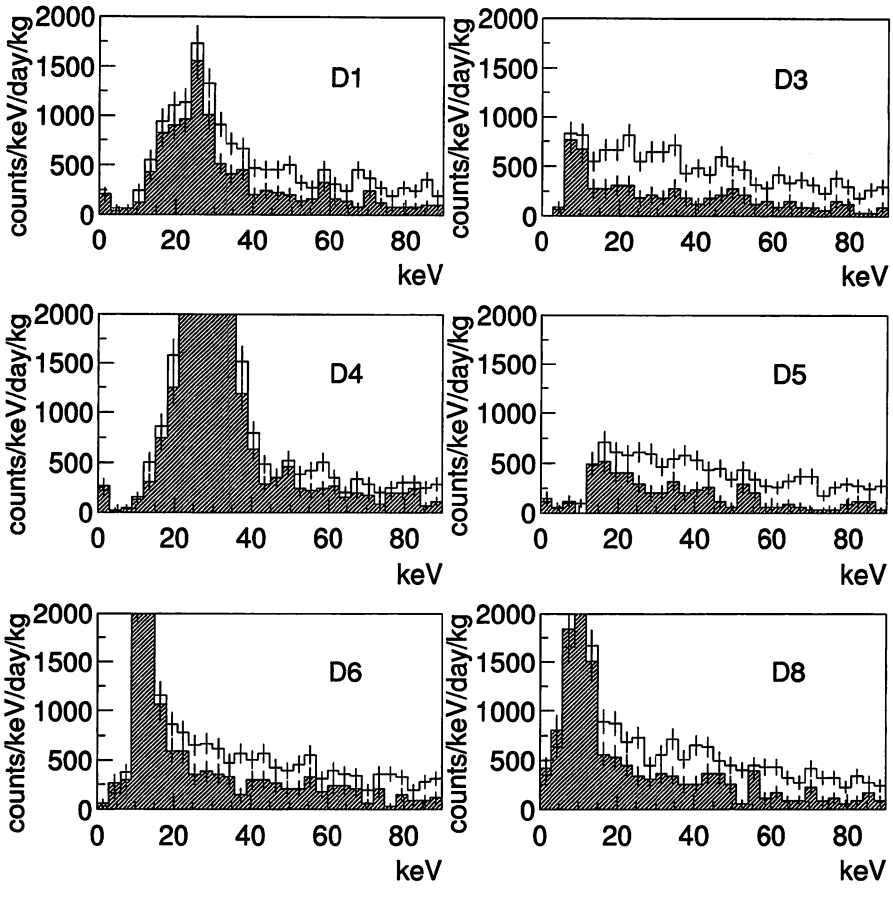

Figure 32: Obtained energy spectra in the first experiment in Nokogiriyama underground cell . The hatched and no-hatched spectra are with and without veto ones, respectively.[34]

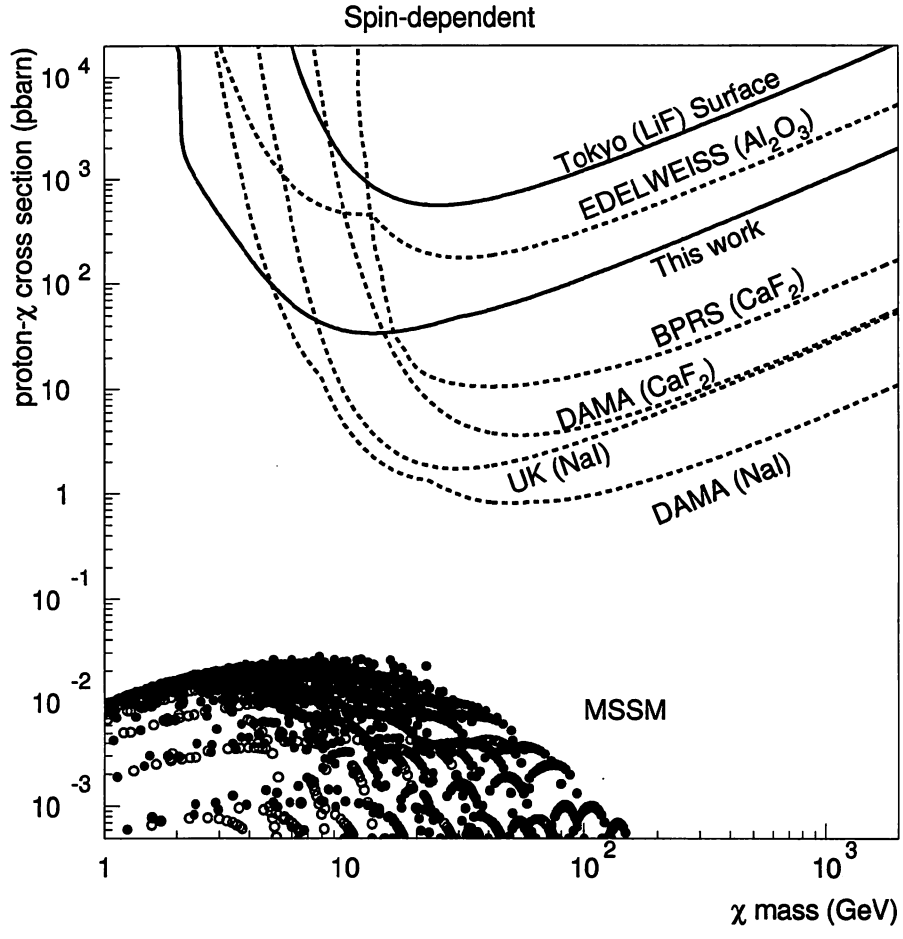

Figure 33: Obtained exclusion limit for the spin-dependently interacting cross section as a function of the neutralino mass. For comparison the exclusion plots derived from the data in [37, 38, 39, 40] and scatter plot predicted in MSSM($10\,\mathrm{GeV} \leq M \leq 1\,\mathrm{TeV}, 10\,\mathrm{GeV} \leq |\mu| \leq 1\,\mathrm{TeV}, 1 \leq \tan\beta \leq 50$, and $m_h = 80$ GeV are also given where small $\tan\beta$ region ($1 \leq \tan\beta \leq 10$) and large $\tan\beta$ region ($10 \leq \tan\beta \leq 50$) are marked with filled and open circles, respectively.[34]

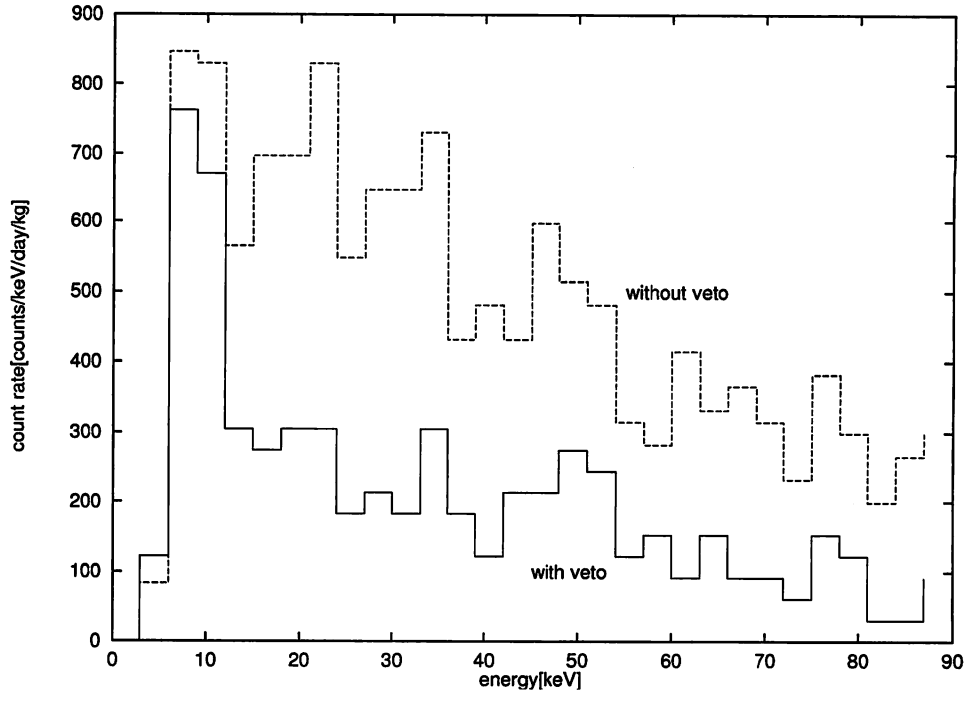

Figure 34: Obtained spectra with LiF bolometer(D3) in the first experiment in Nokogiriyama underground cell.

5 Background Studies(Background Reduction II)

Though we have successfully reduced the background of the LiF bolometer by more than an order of magnitude, much more effort is needed for the dark matter detection. We are planning to perform our experiment in a deeper underground site, but before going to a deeper site, we decided to study the remaining background in Nokogiriyama underground cell and to make some effort for the background reduction.

Obtained spectra near the detector's threshold with and without veto in the first experiment are shown in Figure 34. The count rates are $\sim$ 450 and $\sim$ 170 counts/keV/day/kg averaging over 10–90 keV for without and with veto, respectively.

As a result of our background studies we found that the remaining background has three components: i.e.

- Background due to cosmic ray muons.

- Background due to stray gamma rays.
- Background due to other components.

In this section, we describe the studies and reducing attempts of the three components.

5.1 Background Due to Cosmic Ray Muons

Cosmic ray muons deposit energy to LiF crystal by ionization. Muons also make background by producing neutrons, photons, and electrons in the heavy metal shielding materials. As we will see, the background due to ionization is negligible and the secondary and tertiary particles are contributing largely to the background. The processes are rather intricate and are discussed in [30]. Neutrons, photons, and electrons are produced mainly in following processes:

- Nuclear showers are produced by muons.
- Neutrons are produced by nuclear capture of stopping muons.
- Electrons are produced by muon decay and knock-on by muons.
- Photons are produced by the bremsstrahlung and annihilation of the electrons + positrons.
- High energy photons produce electrons + positrons by pair creation.

As it is not easy to calculate or simulate these process, we evaluated the lower limit of the muon induced background by using the veto efficiency in the high energy region.

5.1.1 Studies on Cosmic Ray Muon Induced Background

From the result of the first experiment, we have learned that the veto system is not adequate. Figure 35 is the spectra in high energy region obtained with the LiF bolometer(D3) with and without veto. The minimum ionization peak caused by cosmic ray muon is seen around 8 MeV, and for the spectrum without veto, the peak due to thermal neutron capture (Eq.38,4.78MeV) is also seen. From these spectra, the veto efficiency in the high energy region(several MeV) is estimated to be $\sim 80\%$.

As we know the muon flux in Nokogiriyama underground cell, we can easily estimate the background in the low energy region due to ionizations of muons. The estimated contribution to the background is ~ 3.6 counts/keV/day/kg and ~ 0.7 counts/keV/day/kg without and with veto, respectively. Here 80% was taken as the veto efficiency.

We also estimated the lower limit of the background due to muon induced particles in the energy region of 10–90keV. We refer to secondary and tertiary

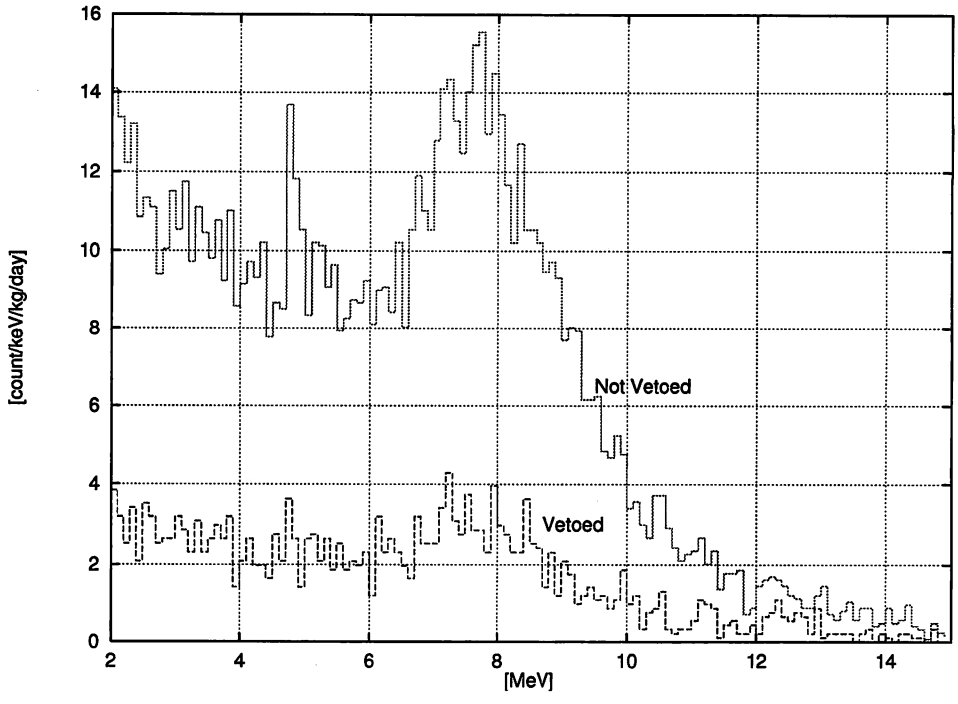

Figure 35: Obtained spectra in the first experiment(D3). The peak around 8 MeV is due to minimum ionizations by cosmic ray muons.

particles produced by muons in the high-Z materials as muon induced particles. The veto efficiency estimated from the minimum ionization peak is thought to be higher than the efficiency in the lower energy region because unvetoed muons can reach the high-Z shieding materials much more easily than they reach the LiF crystals. Thus we can estimate the veto efficiency in low energy region to be less than 80%.

In the energy region of 10–90 keV, the count rates without and with veto are 450 counts/keV/kg/day and 170 counts/keV/kg/day, respectively. The deiffernce, 280 counts/keV/kg/day is the count rate killed by veto and the efficiency is thought to be less than 80%, which claims the muon correlated count rate should have been more than 280/80% = 350 counts/keV/kg/day. Then we find 350-280=70 counts/keV/kg/day is the lower limit of the muon induced particle's contribution to the remaining background in the energy region of 10–90 keV. This study is summarized in Figure 36.

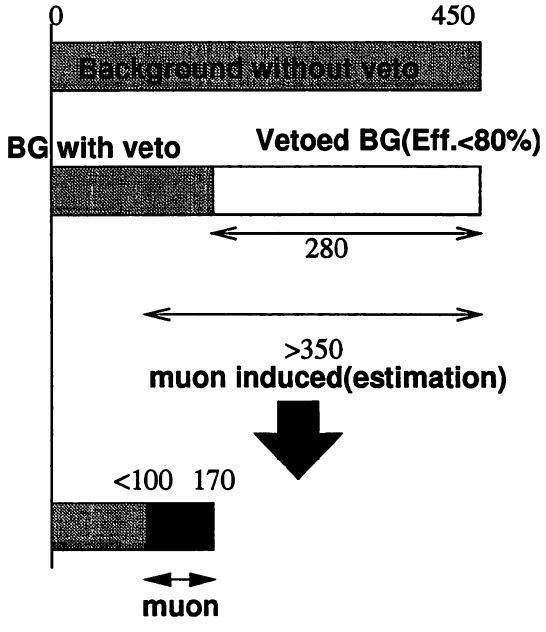

Figure 36: Background(10–90keV) study on muon induced component. The shown figures represent count rate in units of counts/day/keV/kg. 350 = (450-170)/0.8 is estimated lower limit of muon induced contribuion to the unvetoed background. And $350 \times 0.2 = 70$ is the estimated lower limit of muon induced contribuion to the vetoed background.

area	before		after		
	coverage	# of sheets	coverage	# of sheets	effective solid angle
A	83%	3	100%	4	11%
B	56%	5	95%	11	10%
C	100%	12	100%	12	79%
total	90%	20	99%	27	

Table 11: Geometrical coverage of the plastic scintillators in each area. Effective solid angle is defined as solid angle (seen from the detector)$\times$ muon's zenith angle distribution where $\cos^2\theta$ is assumed.

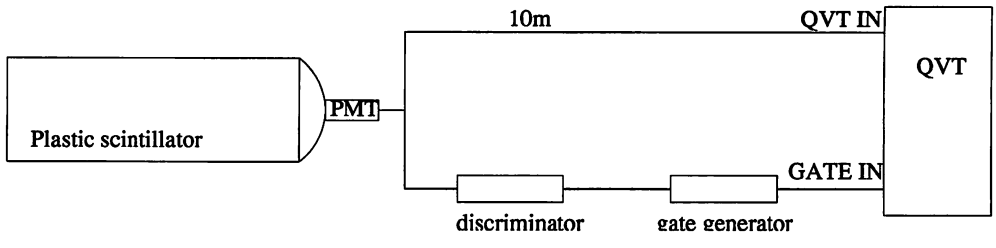

Figure 37: The block diagram of the discrimination adjustment.

5.1.2 Improvement of the Geometrical Coverage

As we discussed in Section 4.5, the geometrical coverage of the plastic scintillators in the first measurement in Nokogiriyama underground cell was about 90 %. The incompleteness of the geometrical coverage is due to the drain of the vacuum tubes and the tube of the helium liquefier. After the first experiment, we managed to add seven sheets of plastic scintillators and the geometrical coverage was raised to 99 %. Geometrical coverage of the veto system before and after the improvement are listed in Table 11.

5.1.3 Re-adjustment of the discrimination level

We re-adjusted the discrimination level of the veto system using a qVt multichannel analyzer Model 3001 by LeCroy research systems. The block diagram of adjusting the discrimination level is shown in Figure 37. We can check the raw spectrum and the spectrum to veto by using internal gate and external gate of the qVt module. The spectra are shown in Figure 38. We set the discrimination level just above the Compton edge of ^{208}Tl.

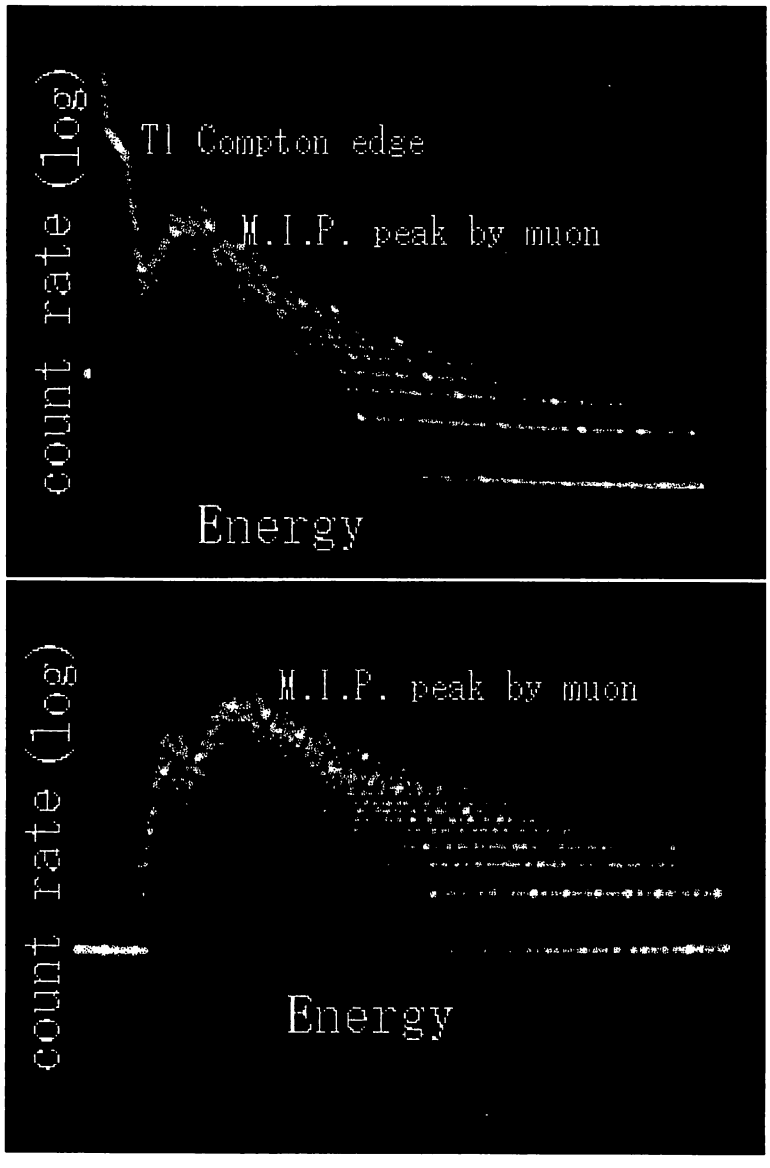

Figure 38: Re-adjustment of the Discrimination Level. Upper spectrum is the raw spectrum and the lower one is the spectrum taken coincidence with the output from the discriminator.

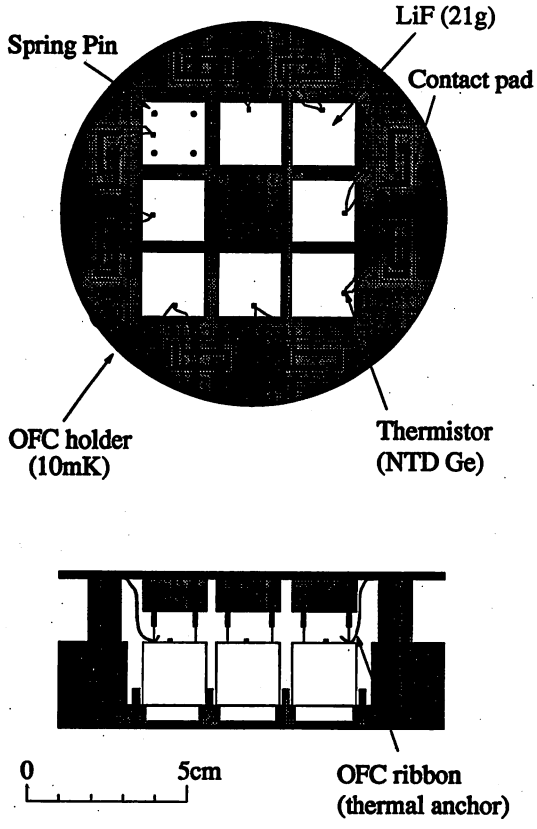

Figure 39: Schematic drawing of the bolometer array use for the second underground experiment. Each LiF crystal is 21g weight.

5.2 Second Underground Experiment

The improvement of the veto system was confirmed with the LiF bolometer. The measurement was performed in Nokogiriyama underground cell , from August 26 to September 2, 1998. In the second underground experiment, each LiF crystals are placed on four copper posts and held with four spring pins for the microphonic noise reduction. Other detector system is same as the first underground experiment. The schematic view of the bolometer array used for the second experiment is shown in Figure 39.

Because of the heat cycle charged to the detector, the thermal contact between the crystal and the thermistor got weak, which caused small signal to noise ratio. Among the six bolometers we could obtain signals, the threshold

of the bolometer which showed best S/N ratio was $\sim$ 30keV. This is not low enough to set a new limit to the neutralino-nucleus cross section. Thus we used the higher energy region for the estimation of the veto efficiency improvement. The veto rate was $\sim$177 Hz and we killed 4 msec after the veto signal. The spectra obtained with the LiF bolometer(D4) are shown in Figure 40. It is seen that the minimum ionization peak is reduced with veto by a factor of 10, that means the veto efficiency was raised from $\sim$ 80% to 90 $\sim$ 93% in the high energy region. The veto efficiency varies according to the geometrical position of the crystal. Statistical error is less than 0.5%. The difference between the geometrical coverage of the veto system($\sim$ 99%) and the veto efficiency($\sim$ 90%) is thought to due to the unexpected defects of the geometrical coverage and muons which deposit energies lower than the discrimination level.

We have improved the geometrical coverage and adjusted the discrimination level and found that 90 % is the upper limit of veto efficiency we can achieve in Nokogiriyama underground cell. All we can do next to reduce muon induced background is going deeper underground.

5.3 Stray Gamma rays

As is shown Figure 28, the detector is not exposed to the outside of the shieldings:i.e. gamma rays cannot hit the detector directly from the outside. But the gamma rays can still reach to the detector by scattering in the copper shielding. We estimated the contribution of the stray gamma rays by EGS4 simulation.

5.3.1 Studies on Stray Gamma Rays

The configuration of the shieldings and the detector used for the simulation is shown in Figure 41. We scaled the calculated gamma ray flux(Sec. B) in the Hongo Campus using the result of the gamma ray flux measurement and used as the gamma ray flux in Nokogiriyama underground cell. Gamma rays were generated on top of the shieldings with a random direction. Spectra around the detector and deposited in LiF crystal are shown in Figure 42. The contribution of the stray gamma rays from the outside of the shieldings was found to be $\sim$ 50 counts/keV/kg/day. Figure 43 summarizes the background studies up to this stage.

We found that the contribution of the stray gamma rays is comparable to that of the cosmic ray muon induced particles. We thought of installing and extra low background lead around the detector and simulated the effect of putting various thickness of lead around the LiF bolometer. The result of the simulation is shown in Figure 44. We learned that with 20mm-thick lead, the stray gamma ray flux is reduced by two orders of magnitude. The internal lead is effective to gamma and beta rays induced by the cosmic rays and from the radioactive contamination inside of the passive shieldings. But if the veto system is not adequate, we might suffer from the background induced by muons within the

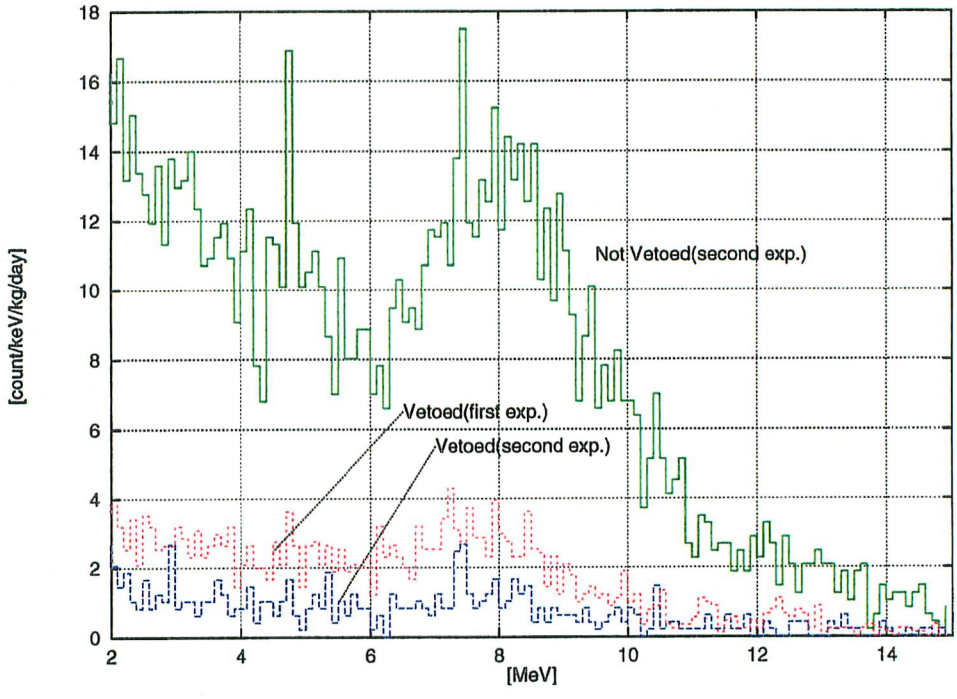

Figure 40: Improvement of the veto efficiency. Obtained spectrum with LiF bolometer without veto, with veto before and after the improvement are shown. The veto efficiency in high energy region was raised from $\sim$ 80% to $\sim$90%.

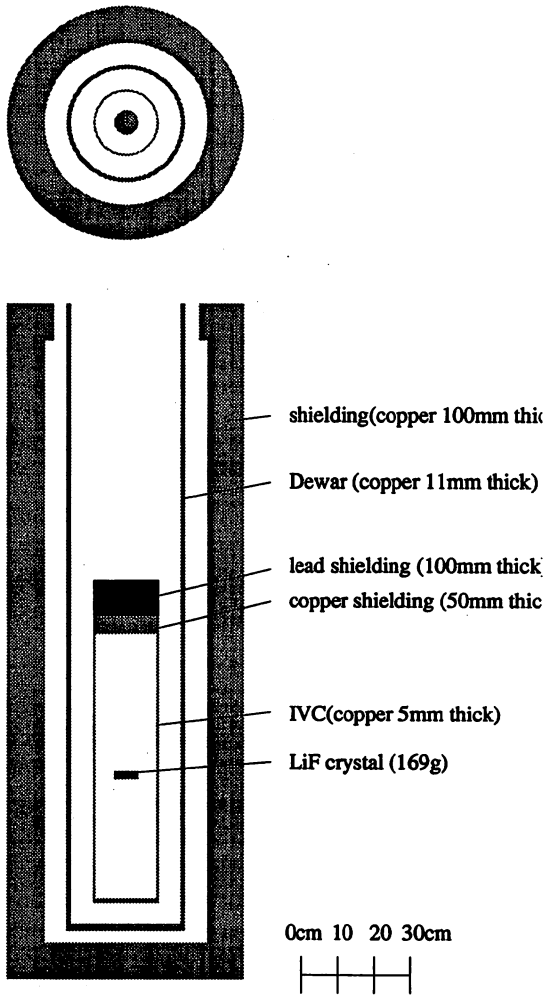

Figure 41: Configuration of the shieldings used for the simulation.

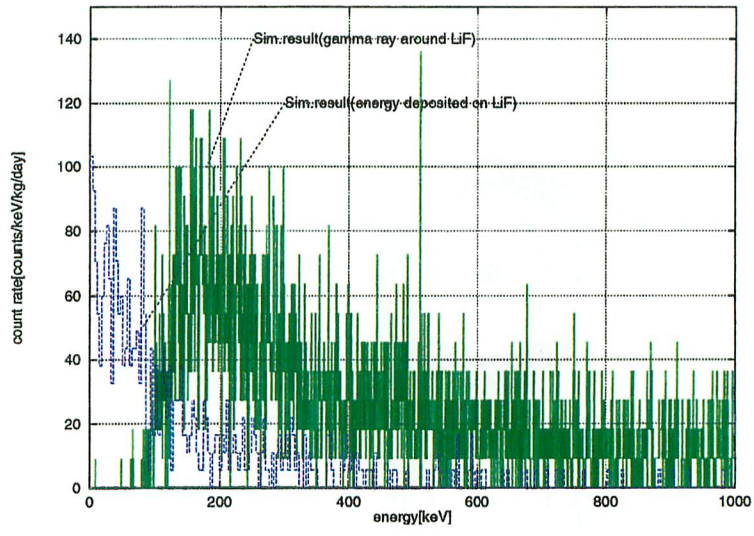

Figure 42: Simulated stray gamma ray spectrum. The spectra around the LiF crystal(solid) and deposited on the LiF crystal(dashed) are shown.

internal lead shielding. In that case, all we can do to eliminate the effect of cosmic ray muons is going deeper underground.

5.3.2 Kanazawa Lead

We learned the effect of installing internal lead shielding by simulation, and we decided to construct an internal shielding. The lead must be very low background because there is nothing to shield the gamma and beta rays from the lead shielding. As we discussed in Section 4.6, lead contains radioactive isotope ^{210}Pb and it is long lived(22.3yr). Radioactive isotopes cannot be removed by chemical purification, so we searched for old lead. We found that professor Komura at Kanazara University possesses some old lead which was used for the Kanazawa castle and is older than 200 years. We were fortunate enough to share 20kg of the old lead.

We measured the Kanazawa lead with HPGe detector and found that contamination of ^{210}Pb, U, Th, and K are all below the detection limit. The obtained spectrum is shown in Figure 45 along with the spectrum of lead C employed for the outer shielding.

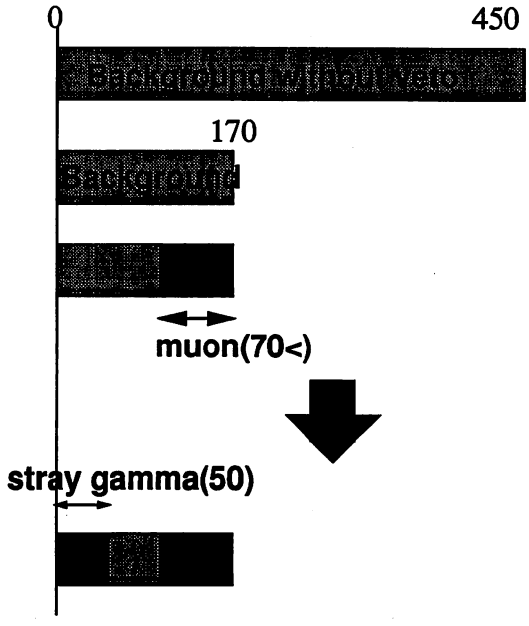

Figure 43: Background study on the stray gamma ray component. The shown figures represent count rate in units of counts/day/keV/kg.

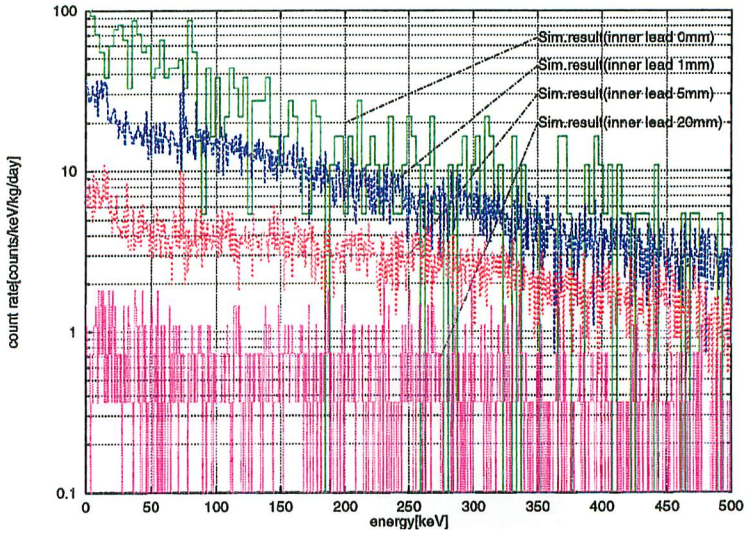

Figure 44: Simulated background spectra deposited on LiF crystal. Results of various thickness of internal shield are shown.

5.3.3 Construction of an Internal Shielding

We have obtained very low background lead, we need to construct the shielding without contaminating it with any radioactive materials. Generally, a mold is made of sand, but sand contains K, whose radioactive isotope ^{40}K(natural abundance 0.0017%) would be a serious background source. We avoided this risk by employing iron, which doesn't make alloy with lead, for the mold material. We selected a dipper made of stainless, which doesn't make alloy with lead, either. The pictures of melting and molding the lead are shown in Figure 46.

As the experimental space is limited in the dilution refrigerator, we needed to design a new holder for the LiF bolometer to install internal lead shielding. The schematic drawing of the newly designed holder and the internal shielding is shown in Figure 47. The new holder consists of 2 modules of bolometer array, each module holds 4 LiF crystals. Each LiF crystal is supported with 4×6 spring pins to reduce the microphonic noise. The pictures of the new holder are shown in Figure 48 and 49.

5.4 Studies on Other Background Components

Although the materials used in the dilution refrigerator are carefully selected, some components are found to have certain amount of radioactive contamination[36]. We estimated the contribution of these materials based on the measured con-

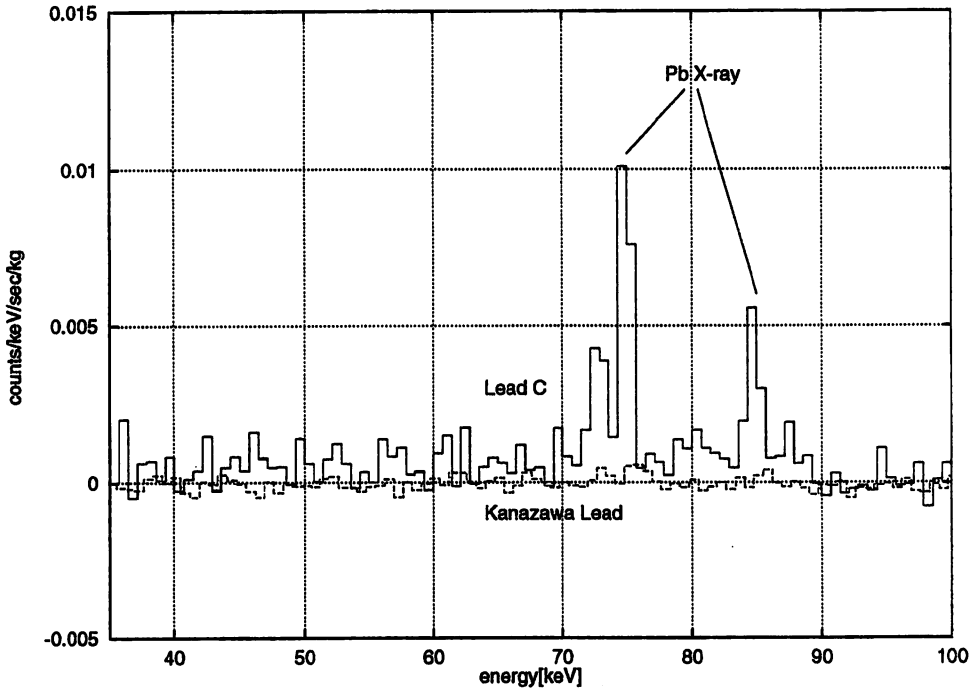

Figure 45: The spectrum of the Kanazawa lead obtained with HPGe detector. The spectrum of the lead C, which was used for the passive shieldings, is also shown.

Figure 46: Pictures of melting and molding Kanazawa lead.

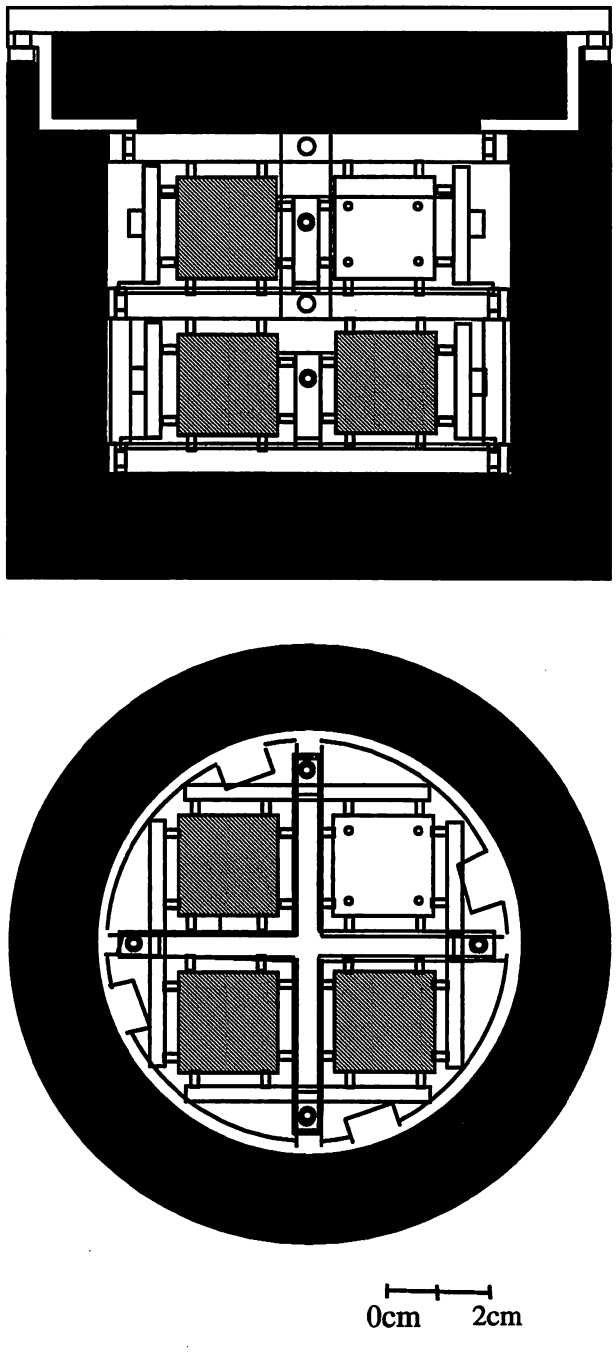

Figure 47: Schematic drawing of the new holder and internal shielding.

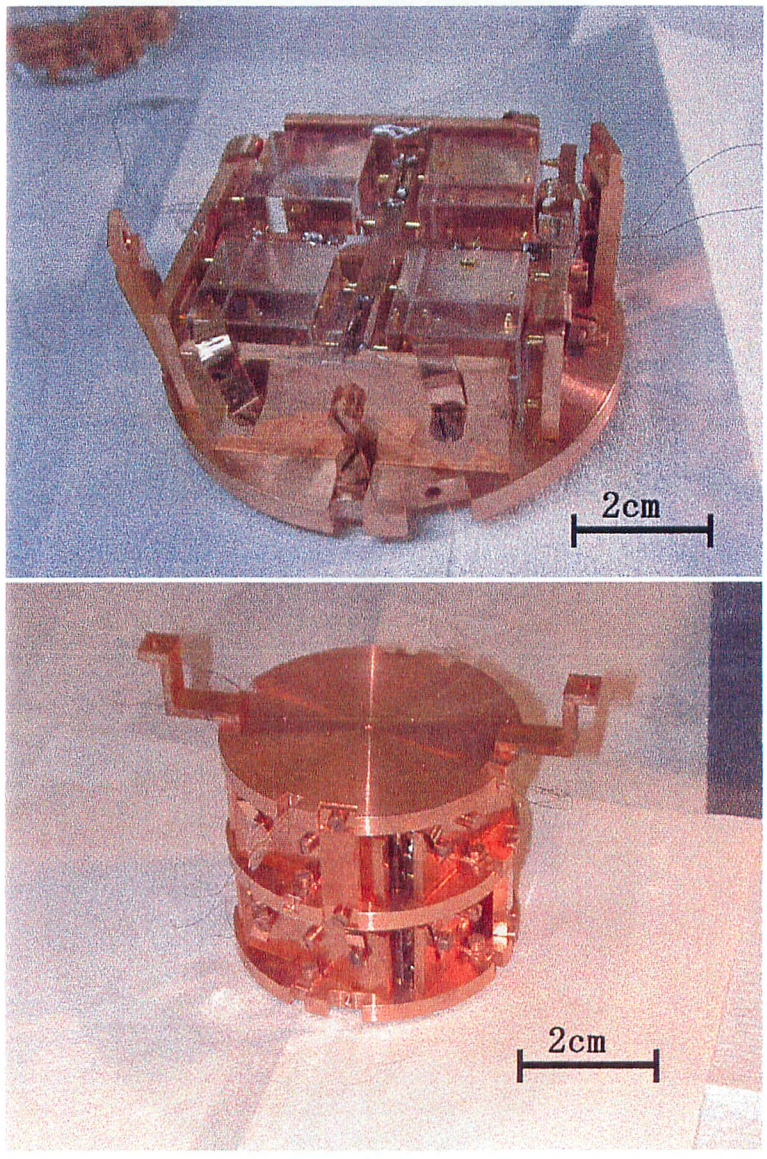

Figure 48: New detector holder and LiF crystals.

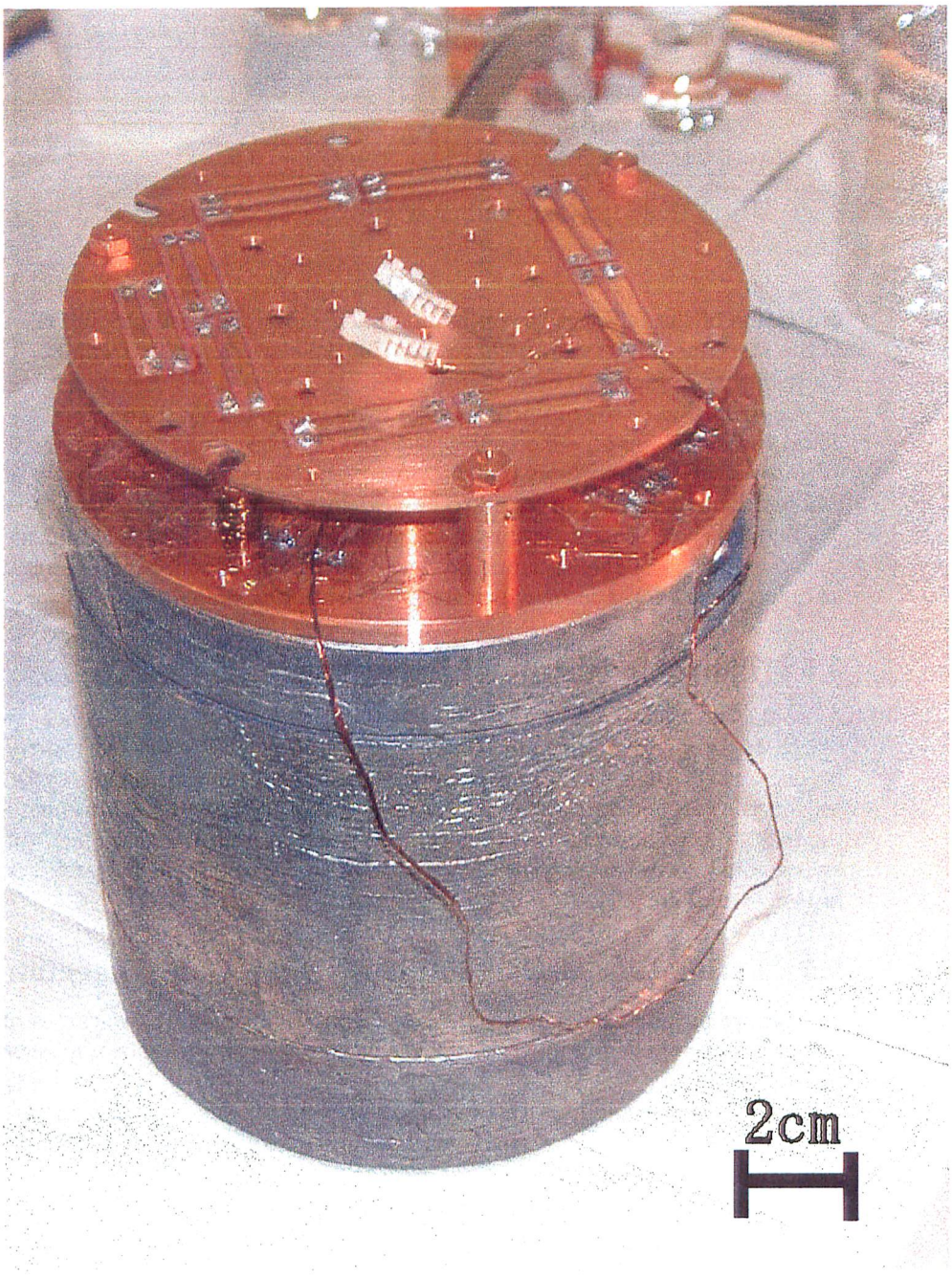

Figure 49: Constructed internal lead shielding. The shielding is 20mm thick, 128mm diameter, and 130mm height.

material	count rate[counts/keV/day/kg]
FRP	2.2
stainless	< 0.6
resistor	< 0.1
fast neutron(ambient)	~ 0.5

Table 12: Contribution of other background sources.

centration of the radioactive contamination, geometrical position, and the mass of the material. Materials and their contributions are shown in Table 12. These contributin are found to be negligible.

Contribution of the ambient neutrons was estimated by simulation[35]. The count rate is $\sim$ 2.8 and $\sim$0.5 counts/keV/day/kg averaging the energy region of 10–90keV with and without the shielding, respectively. The contributin of the ambient neutrons is again found to be negligible.

Though the fast neutron flux in the shielding is larger than the ambient one, the contribution of the neutrons produced in the high-Z materials are regarded as muon induced particles, which we have already discussed.

5.5 Third Underground Experiment

After the construction of the internal shielding, we tried to perform dark matter search experiment in Nokogiriyama underground cell. We started the cooling November 11, 1998. During the cooling procedure, we found that there is a leak in the $^3He - ^4He$ line. It was impossible to perform the experiment with the leak. As we had planned to check the whole system in the Hongo campus before going deeper underground, we decided to repair the dilution refrigerator in Hongo campus.

5.6 Estimation of Current Sensitivity of our Detector

Though we haven't confrim the effect of the internal shielding, we can estimate the sensitivity of the bolometer using the background studies shown in Table 13 and Figure 50.

By the improvement of the veto system, veto efficiency is now more than 90%. The contribution of stray gamma rays and other gamma rays will be reduced by two orders of magnitude with the internal lead shielding.

Although there are some unknown components, we can estimate the current sensitivity of our detector on the assumptions that

- assumption A; all of the unknown components are muon induced background.

source	count rate[counts/keV/kg/day]
background with veto	170
muon induced	> 70
stray gamma	~ 50
other	~ 5
unknown	< 45

Table 13: Result of background studies.

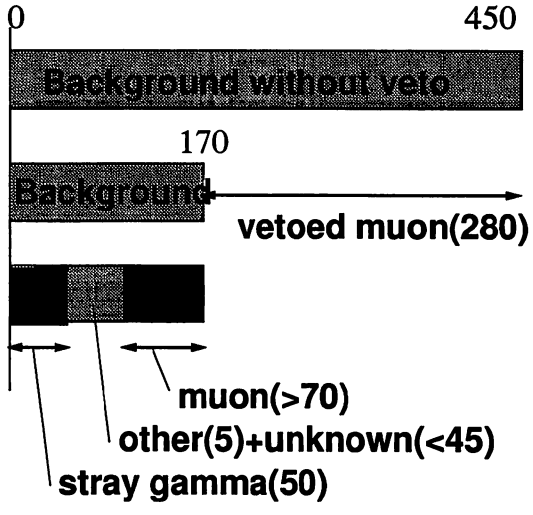

Figure 50: Result of the background(10–90keV) studies.

- assumption B; all of the unknown components are gamma rays.

On assumption A, 55 counts/keV/kg/day of gamma rays and 395 counts/keV/kg/day of muon induced particles make 450 counts/keV/kg/day which is the unvetoed background. Then 55×0.01(shielding)$+395\times0.1$(veto) $=$ 40 counts/keV/kg/day is the expected count rate.

On assumption B, 100 counts/keV/kg/day of gamma rays and 350 counts/keV/kg/day of muon induced particles make 450 counts/keV/kg/day. Then 100×0.01(shielding)$+$ 350×0.1(veto) $=$ 36 counts/keV/kg/day is the expected count rate.

These estimations indicate the sensitivity should be improved by a factor of $4 \sim 5$ compared to the first experiments in Nokogiriyama underground cell, which indicates that our detector is sensitive to the spin-dependntly interacting cross section down to $\sim$10pbarn for neutralino with mass 10GeV.

We further need to think of the effect of the internal shielding to the muon induced particles. The internal shielding reduces the muon induced particles by two orders of magnitude, while muons also produce background source within the internal shielding. Estimation of the latter component is difficult. If the muon induced background is reduced by an order of magnitude on average, the count rate will be $4 \sim 5$counts/keV/kg/day.

If the second assumpiton on the effect of internal shielding to the muon induced particles were right, the sensitivity of our detector would have improved by a factor of $30 \sim 40$ compared to the first experiments in Nokogiriyama underground cell, which indicates that our detector is sensitive to the spin-dependently interacting cross section down to $\sim$1pbarn for neutralino with mass 10GeV.

6 Future Prospects

As we need to repair the dilution refrigerator and check the stability of the whole system before going deeper underground, we first bring back the whole detector system back to the Hongo campus of University of Tokyo. As we found in section 4.2, the muon flux in the Hongo campus of University of Tokyo is only three times as high as that of in Nokogiriyama underground cell, we can expect an improved result in the Hongo campus with improved veto efficiency, internal shielding, and new crystal holders that are already prepared. After the check running in the Hongo campus of University of Tokyo, we are going to install the detector system in an underground cell with sufficient depth($>$ 2000m.w.e.). Background due to the cosmic ray muon will be negligible, then stray gamma ray will be the dominant background source, which is expected to be reduced more than two orders of magnitude. We can expect our detector will be sensitive to the spin-dependently interacting cross section down to $\sim$0.4 pbarn for neutralino with mass 10GeV.

After that, with sufficient background study and development, we will bring our detector's sensitively for the spin-dependent interaction below $\sigma_{\mathrm{S.D.}}(\chi-\mathrm{p}) <$ 0.01pb which is comparable to the cross section predicted by the SUSY model.

	Hongo	Nokogiriyama	ratio(Noko/Hongo)
muon flux[$cm^{-2}s^{-1}$]	1.1×10^{-2}	3.4×10^{-3}	0.32
gamma ray flux[$cm^{-2}s^{-1}$]	1.5	2.2	1.5
thermal neutron flux[$cm^{-2}s^{-1}$]	1.9×10^{-3}	9.4×10^{-5}	2.0×10^{-2}
fast neutron flux[$cm^{-2}s^{-1}$]	1.2×10^{-2}	4.9×10^{-4}	2.4×10^{-2}

Table 14: Muon, gamma ray, and neutron fluxes measured in Nokogiriyama underground cell and in the surface.

background source	count rate[counts/keV/day/kg]
muon	> 70
stray gamma	~ 50
other	< 5
unknown	< 45

Table 15: Result of background studies.

7 Conclusions

We measured the muon, gamma ray, and neutron fluxes in Nokogiriyama underground cell. The results are listed in Table 14. We then designed an appropriate shieldings and veto system for the pilot running of the dark matter detection experiments in Nokogiriyama underground cell. By installing our experimental facilities in Nokogiriyama underground cell, we have successfully reduced the background of the LiF bolometer by more than an order of magnitude. From the obtained spectra the exclusion limits for the cross section of the elastic neutralino-proton scattering as a function of neutralino mass are derived. For spin-dependent interaction, the limits for the neutralino with a mass below 5 GeV are improved.

We studied the remaining background and found that it consists of mainly two conponents. The result is shown in Table 15. For the background reduction, we improved the veto efficiency and have checked the improvement with the LiF bolometer. The veto efficiency was raised from $\sim 80\%$ to $\sim 90\%$. We then studied the stray gamma ray originated background by simulation and found that it can be reduced by two orders of magnitude if we install internal lead shielding with thickness of 2cm. We constructed an internal shielding with very low background 200-year-old lead. During the cooling procedure of the third experiment, we found a leak in the dilution refrigeraor and heven't confirmed the effect of the internal shielding yet.

Acknowledgements

I wish to first thank my adviser Prof. Minowa for his excellent guidance, support, and patience. I am grad to have learned and to have some years ahead to learn various things from his broad knowledge on physic and other things.

I want to thank Dr. W.Ootani for his instruction on the whole experiment. Without his advice, this thesis could not be completed.

I want thank my collaborators: Y. Inoue, Dr. T. Watanabe, Dr. Y. Ito, Dr. S. Moriyama, A. Takeda, and Prof. Y. Ootsuka for many useful discussions and good advice.

I want to express my gratitude to Prof. Komura at Kanazawa University for offering 25kg of very low background lead. Though we haven't confirmed the effect of the lead, it will play a very important role in the near future stage of our experiments.

I want to thank International Center for Elementary Particle Physics(ICEPP) for allowing me to use their workstations, facsimile, library and so on. I would like to thank S. Otsuka for his advice and support of our engineering work.

I want to thank other members of Minowa group, T. Namba and Y. Takasu for their helpful discussions.

A Home Made Dilution Refrigerator

For the dark matter detection experiment, we have constructed a dilution refrigerator with low activity materials. The picture of the refrigerator is shown in Figure 51.

A.1 Principle of Dilution Refrigerator

The liquid mixture of ^{3}He and ^{4}He is in the mixing chamber shown in Figure 52. Phase separation takes place in the mixing chamber and the temperature of the mixing chamber goes down to $\sim$ 10mK. The cooling is caused by ^{3}He evaporating from the ^{3}He concentrated phase into the ^{3}He dilute phase. The concentrated phase floats on the dilute phase. The continuos cooling is achieved by circulating the ^{3}He gas by a vacuum pump. Heat exchange is important to obtain certain cooing power and as shown in Figure 52, the incoming ^{3}He gas is cooled by the outgoing ^{3}He gas in the heat exchanger. Schematic diagram of a dilution refrigerator is shown in Figure 53.

B Low Background HP Germanium Detector

The materials used for the construction of the detector and dilution refrigerator are carefully selected from the viewpoint of radioactive contamination. The measurement was performed with a low-background germanium gamma

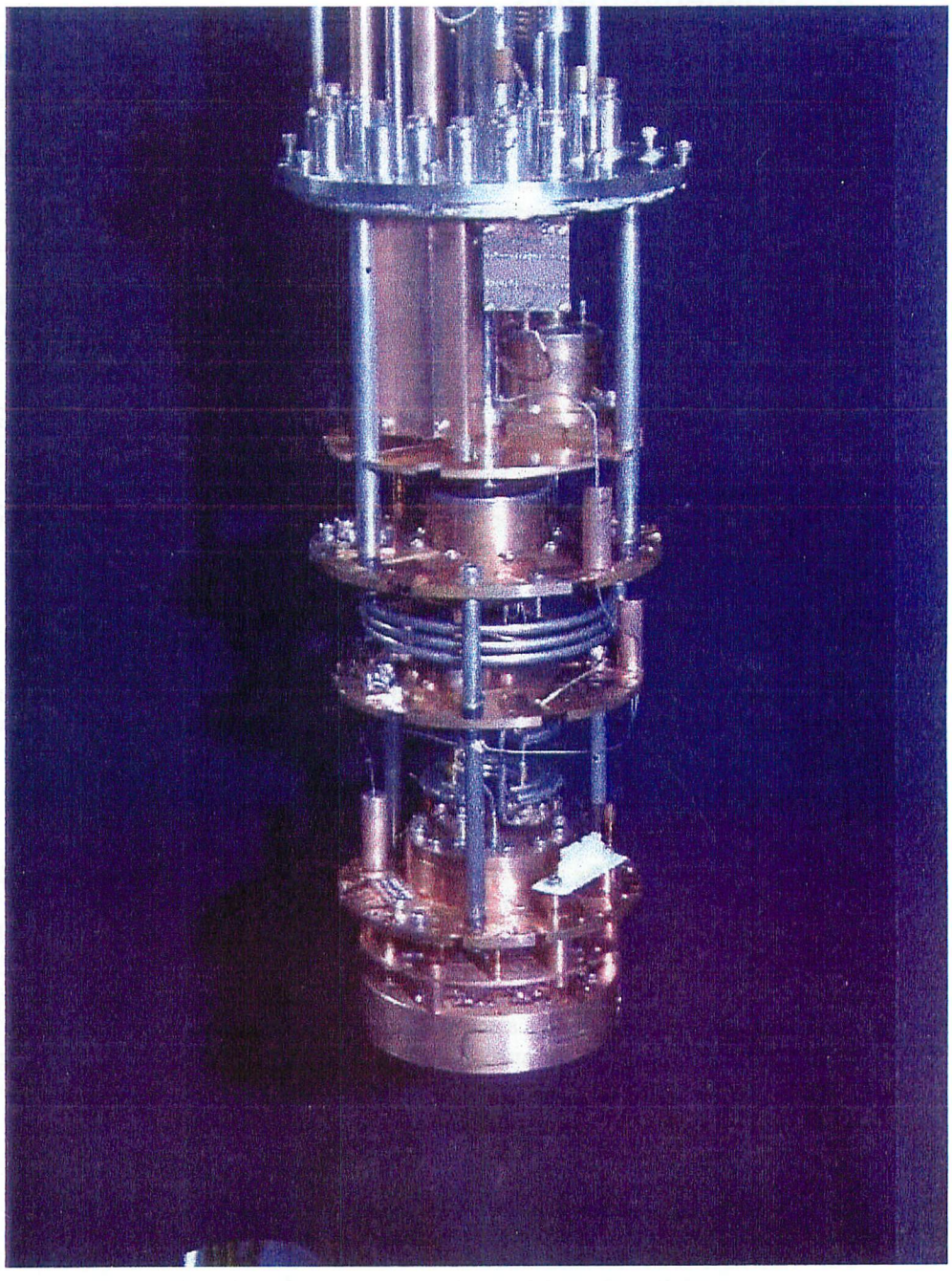

Figure 51: Dilution refrigerator constructed for the dark matter detection experiment.

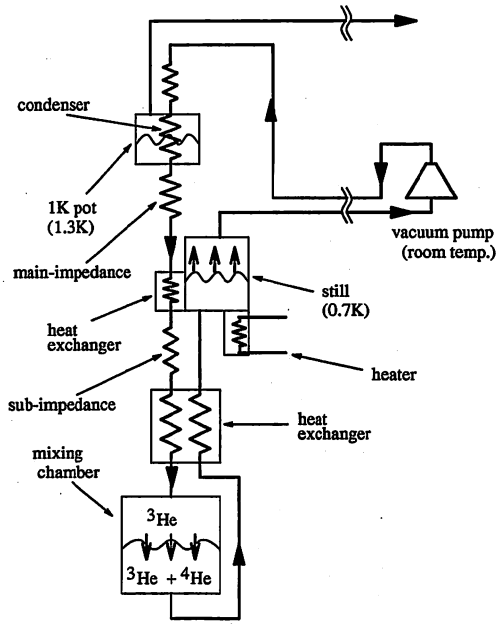

Figure 52: Diagram of ^{3}He – ^{4}He dilution refrigerator.

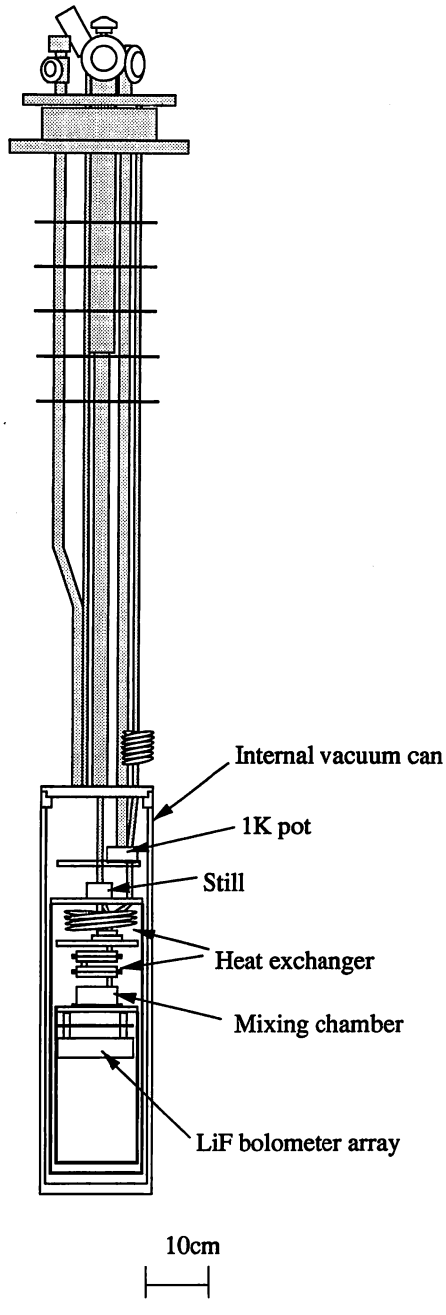

Figure 53: Schematic drawing of the constructed dilution refrigerator.

ray spectrometer(HPGe detector). The detector is EG&G ORTEC High-Purity Germanium coaxial detector system GEM-25195. The p-type germanium crystal has dimensions 57.1mm in diameter and 54.6mm in length (134cc) and is enclosed in a nickel-plated magnesium cylinder. The relative detection efficiency relative to that of a 3" × 3" NaI(Tl) scintillator at 1333 keV is 30.2%. The energy resolution (FWHM) is 1.95 keV for 1333 keV line of ^{60}Co and 0.83 keV for 122 keV line of ^{57}Co. The detector is operated in the Hongo campus of University of Tokyo and is shielded with 7.5cm-thick inner copper layer and 15cm thick of outer lead layer. Figure 54 shows the schematic drawing of the HPGe detector system. Inside of the OFHC is purged with gas nitrogen[41]. The background spectra obtained by the HPGe detector with the shieldings are shown in Figure 55.

The background was also measured without shieldings and the gamma ray flux was calculated[42]. The calculated ambient gamma ray spectrum is shown in Figure 56. The estimated gamma ray flux is 1.5cm^{-2}s^{-1}.

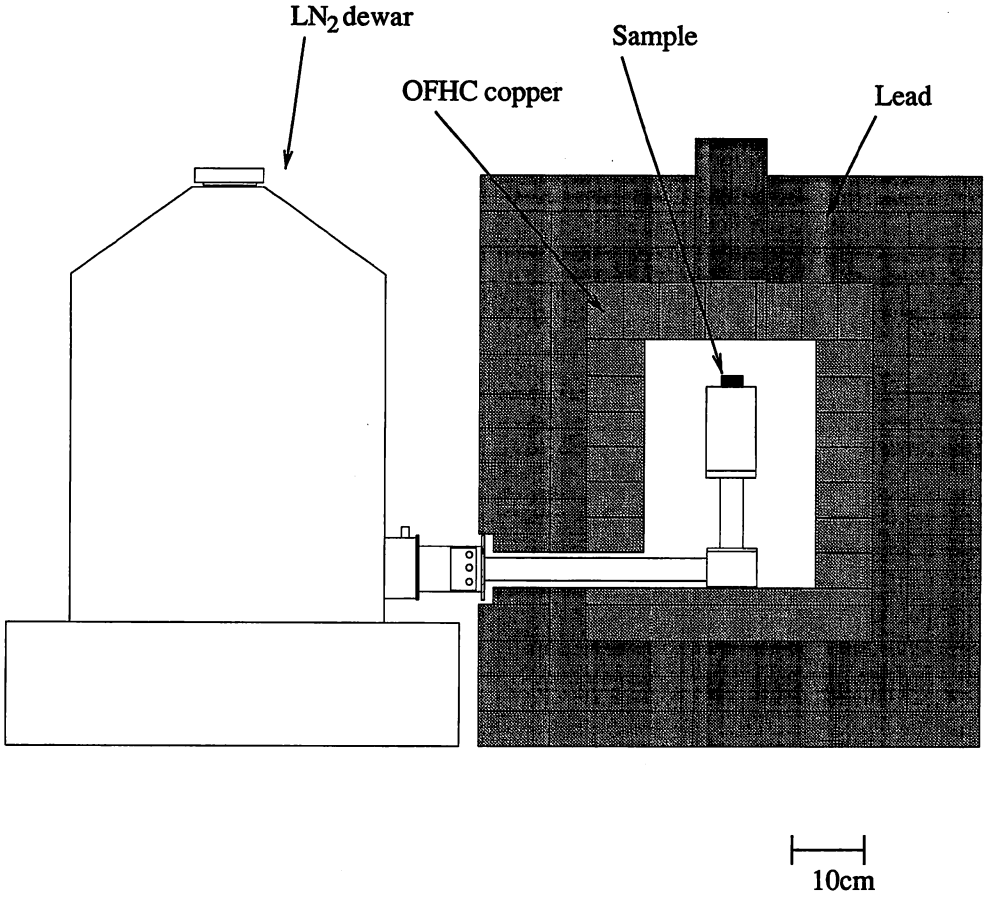

Figure 54: Schematic drawing of low-background HPGe detector. The shieldings consist of 7.5cm-thick inner OFHC copper layer and 15cm-thick outer lead layer.

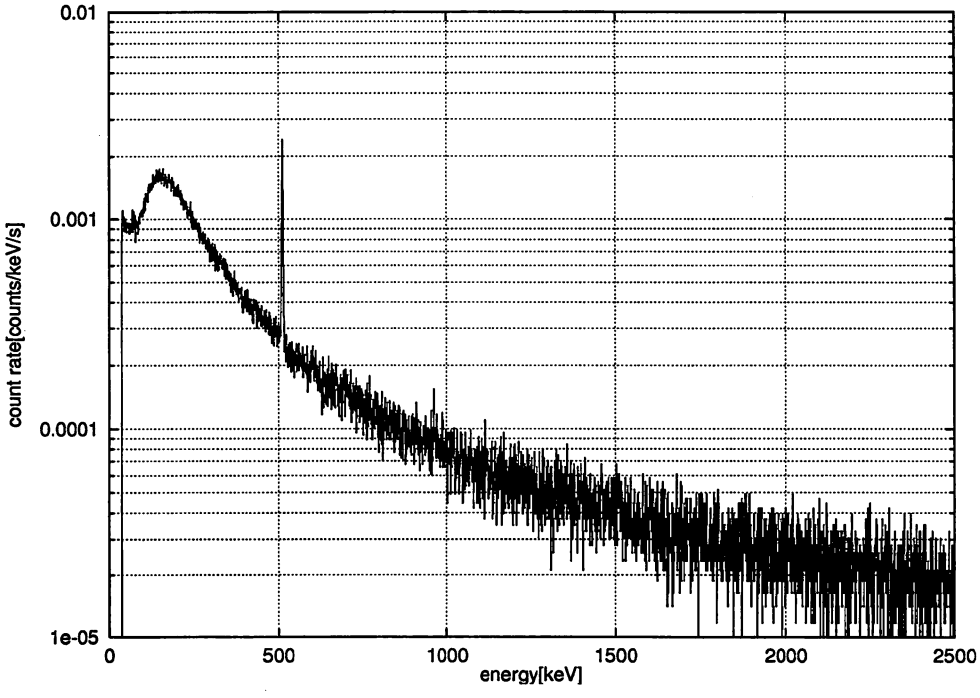

Figure 55: Background spectrum obtained by HPGe detector. Live time is 6.0×10^5sec.

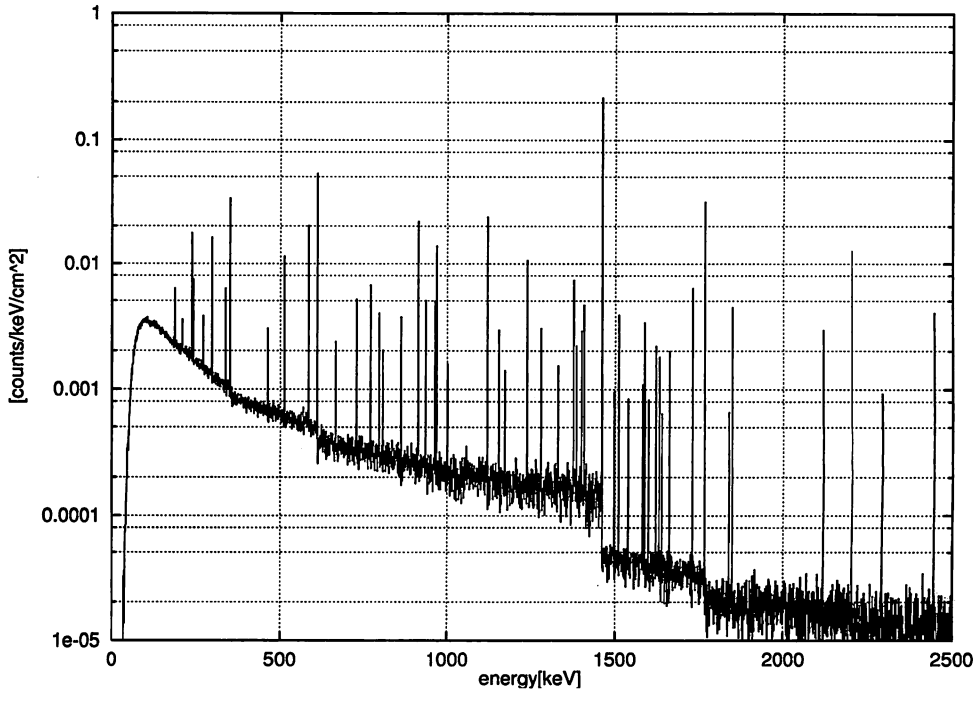

Figure 56: Simulated ambient gamma ray apectrum.

References

[1] M. Fich and S. Tremaine, Annu. Rev. Astron. Astrophys. **29**(1991)409.

[2] E. Auborg , preprint DAPNIA/SPP 92-22.

[3] David N. Schrarmm and Michael S. Turner, Reviews of Modern Physics **70**(1998)303.

[4] Scott Burles and David Tytler, Astrophys. J. **480**(1998)6

[5] B. Paczynski Astrophys. J. **304**(1986)109.

[6] J. V. Narlikar and T. Padmanbhan, Annu. Rev. Astron. Astrophys. **29**(1991)325.

[7] A. Milsztajn, Nucl. Phys. B **35**(1994)137; E. Aubourg *et al.*, Nature **365**(1993)623; L. Moscoso, Nucl. Phys. B (Proc. Suppl.) **38**(1995)387.

[8] C. Alcock *et al.*, Nature **365**(1993)621; B. Sadoulet, Nucl. Phys. B (Proc. Suppl.) **35**(1994)117; W. Sutherland, Nucl. Phys. B (Proc. Suppl.) **38**(1995)379.

[9] A. Udalski *et al.*, Acta Astron. **43**(1993)289.

[10] A. N. Taylor and M. Rowan-Robinson, Nature **359**(1992)396.

[11] Super-Kamiokande Collaboration, Phys. Rev. Let. **81**(1998)1562.

[12] R. D. Peccei and H. R. Quinn, Phys. Rev. Lett. **38**(1977)1440.

[13] Michael S. Turner, astro-ph/9811364, astro-ph/9811366.

[14] T. Mori, Proc. of the 2nd RESCEU International Symposium on "Dark Matter in the Universe and its Direct Detection", November 26-28,1996, University of Tokyo.

[15] J. D. Lewin and P. F. Smith, Astropart. Phys. **6**(1996)87.

[16] R. Bernabei, *Researches on Dark Matter*, La Rivista del Nuovo Cimento della Societa Italiana di Fisica 1995.

[17] P. F. Smith and J. D. LEWIN, *Dark Matter Detection*, Rutherford Appleton Laboratory, Chilton, Oxon., England.

[18] E. I. Gates, G. Gyuk and M. S. Turner, Astrophys. J. **449**(1995)L123.

[19] J. Ellis and R. A. Flores, Nucl. Phys. B**307**(1988)883.

[20] G. Eder, *Nuclear Forces* (MIT Press, 1968), Chapter 7.

[21] The OPAL Collaboration, hep-ex/9809031

[22] A. Alessandrello *et al.*, Phys. Lett. B**408**(1997)465.

[23] N. J. C. Spooner *et al.*, Phys. Lett. B **321**(1994)156.

[24] G. J. Davies *et al.*, Phys. Lett. B **322**(1994)159.

[25] R. Hazama, doctorial thesis, the Osaka University graduate school of science Toyonaka, Osaka, 1998.

[26] Y.Messous *et al.*, Astropart. Phys. **3**(1995)361.

[27] G.Gerbier *et al.*, Phys. Rev. D **42**(1990)3211.

[28] W. Ootani *et al.*, Nucl. Instr. Meth. A **372**(1996)534.

[29] W. Ootani *et al.*, Astropart. Phys. **9**(1998)325.

[30] G. Heusser, Nucl. Instr. Meth. B **83**(1993)223.

[31] *Table of Isotopes,* seventh edition, edited by C. M. Ledere and V. S. Shirley (JOHN WILEY & SONS, INC., New York Chichester Brisbane Toronto,1978).

[32] Donald J. Hughes and Robert B. Schwart, *Neutron Cross Sections.*

[33] Y. Uwamino and T. Nakamura, Nucl. Instr. Meth. A **239**(1985)299.

[34] W. Ootani, doctorial thesis, University of Tokyo,1998.

[35] Y. Kishimoto, master thesis, University of Tokyo, 1996.

[36] K. Nishigaki, master thesis, University of Tokyo, 1995.

[37] A. de Bellefon *et al.*, Astropart. Phys.**6**(1996)35.

[38] C. Bacci *et al.*, Astropart. Phys.**2**(1994)117.

[39] R. Bernabei *et al.*, Astropart. Phys. **7**(1997)73;
R. Bernabei *et al.*, Phys. Lett. B **379**(1996)73.

[40] P. F. Smith *et al.*, Phys. Lett. B**379**(1996)299.

[41] This improvement was done by A. Takeda.

[42] This simulation was performed by T. Namba.